The Planetary Science Journal, 3:31 (39pp), 2022 February https://doi.org/10.3847/PSJ/ac3087

Planet Four: Derived South Polar Martian Winds Interpreted Using Mesoscale Modeling

Ganna Portyankina[1], Timothy I. Michaels[2], Klaus-Michael Aye[1], Megan E. Schwamb[3,4], Candice J. Hansen[5], and Chris J. Lintott[6]
[1] Laboratory of Atmospheric and Space Physics, University of Colorado in Boulder, Boulder, CO 80303, USA; Ganna.Portyankina@lasp.colorado.edu
[2] SETI Institute, 189 Bernardo Ave., Suite 200, Mountain View, CA 94043, USA
[3] Astrophysics Research Centre, School of Mathematics and Physics, Queen's University Belfast, Belfast BT7 1NN, UK
[4] Gemini Observatory, Northern Operations Center, 670 North A'ohoku Place, Hilo, HI 96720, USA
[5] Planetary Science Institute,1700 East Fort Lowell, Suite 106, Tucson, AZ 85719, USA
[6] Oxford Astrophysics, Denys Wilkinson Building, Keble Road, Oxford OX1 3RH, UK
Received 2020 October 21; revised 2021 July 23; accepted 2021 August 16; published 2022 February 4

Abstract

For the first time, model-derived and imagery-derived wind directions and speeds have been compared in Mars's south polar region. Seasonal fan-shaped deposits are routinely observed by HiRISE in the polar regions. They are widely accepted to result from CO_2 gas jet eruptions. Fan lengths, sizes, and shapes can provide information about wind directions and strengths at the times such eruptions occur. We utilize a catalog of those fan-shaped deposits, marked by citizen scientists within the framework of the Planet Four (P4) project, at 27 regions of interest (ROIs) for two spring seasons (Mars years 29 and 30). Fans change considerably from one HiRISE image to another at most of these ROIs as wind direction changes over the spring season. Leveraging this characteristic, intraseasonal variations in near-surface wind speeds and directions were retrieved and compared to near-surface winds predicted by a mesoscale atmospheric model (MRAMS) at the same ROIs. At most ROIs P4-inferred wind directions are consistent with those from MRAMS. The P4-derived wind speeds are less constrained but are consistent with MRAMS wind speeds at the majority of ROIs. The overall consistency between the P4-inferred and MRAMS wind directions supports the underlying assumption that fan formation is controlled by the wind and is not simply due to ballistic trajectories of material exiting suitably nonvertical vents. Measurements of seasonal fan-shaped deposits in HiRISE imagery can thus provide important intraseasonal information about near-surface winds—invaluable for both validating climate modeling and quantitatively investigating Mars's polar processes.

Unified Astronomy Thesaurus concepts: Mars (1007); Seasonal phenomena (1437); Planetary atmospheres (1244)

Supporting material: figure sets, machine-readable table

1. Introduction

Mars is host to a unique springtime process with no earthly analog. Every fall a broad seasonal cap of CO_2 frost forms via surface deposition and/or snow in Mars's higher latitudes (Leighton & Murray 1966; Hayne et al. 2014), annealing into solid ice over the winter (Matsuo & Heki 2009). Images from the Mars Observer Camera (MOC) on the Mars Global Surveyor spacecraft (Malin et al. 1992) were the first to show the exotic nature of the sublimation of Mars's seasonal CO_2 caps in the spring. Fans of dark material were observed on top of the seasonal polar caps, and in the south polar regions, radially organized channels (araneiforms or "spiders") eroded into the underlying surface were detected (Malin & Edgett 2007; Piqueux et al. 2003). To explain both phenomena, Kieffer (Kieffer et al. 2006; Kieffer 2007) postulated that an impermeable layer of CO_2 slab ice forms every winter. In the spring sunlight penetrates the translucent ice and warms the ground below. Some ice sublimates from the bottom of the slab, and the resulting gas is trapped under increasing pressure, eventually rupturing the ice and escaping, creating a cold CO_2 jet that entrains material eroded from the ground below the seasonal ice. The entrained particulates fall onto the top surface of the ice in fan-shaped deposits, oriented by the ambient wind. We refer to this as the "Kieffer process." This process can occur more than once per spring season in the same location. The fan deposits themselves are not observable after mid-summer, when the seasonal CO_2 ice slab fully sublimes away, as they are of the same composition as the substrate. Thus, the fans record the spring season's winds. The High Resolution Imaging Science Experiment (HiRISE; McEwen et al. 2007) on the Mars Reconnaissance Orbiter (MRO) has the capability to routinely point off-nadir to get repeat imaging of south polar region targets in southern spring and summer, as well as a high signal-to-noise ratio that enables imaging when the Sun is low on the horizon at the very beginning of the seasonal activity. HiRISE images, acquired over >7 Mars years (MY) at multiple times during the spring at a set of monitoring sites, have enabled the study of the spring sublimation process and have largely substantiated the Kieffer process hypothesis (Hansen et al. 2010; Portyankina et al. 2010; Thomas et al. 2010, 2011; de Villiers et al. 2012).

Figure 1 shows a subframe of a HiRISE image with a typical example of the fan-shaped deposits of fine material lying on top of the seasonal ice layer. Like windsocks, the directions of the fans are determined by the prevailing wind direction(s) at the time the particulates were injected into the atmosphere from vents in the CO_2 ice (Kieffer et al. 2006). The fan deposits would thus be a record of the wind direction at the time of the release, and the fans could then be used to infer both the local springtime meteorology and interannual variability over several Mars years. Although jets could conceivably be emanating

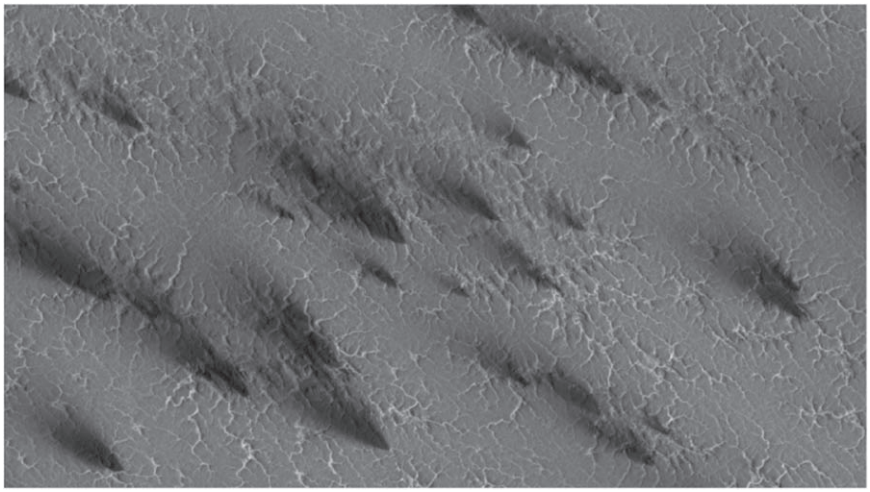

Figure 1. This subframe of HiRISE image ESP_055604_0930 (at 86.89 °S, 170.5 °E) was acquired early in southern spring at $L_s \approx 188.^{\circ}9$. The entire scene, ∼1.5 km in width, is covered by a layer of translucent CO_2 ice. The dark streaks in the image are fan-shaped deposits formed by cold CO_2 jets, and the channels are araneiforms formed by sub-ice erosion during repeated jet outgassing over thousands of Martian years.

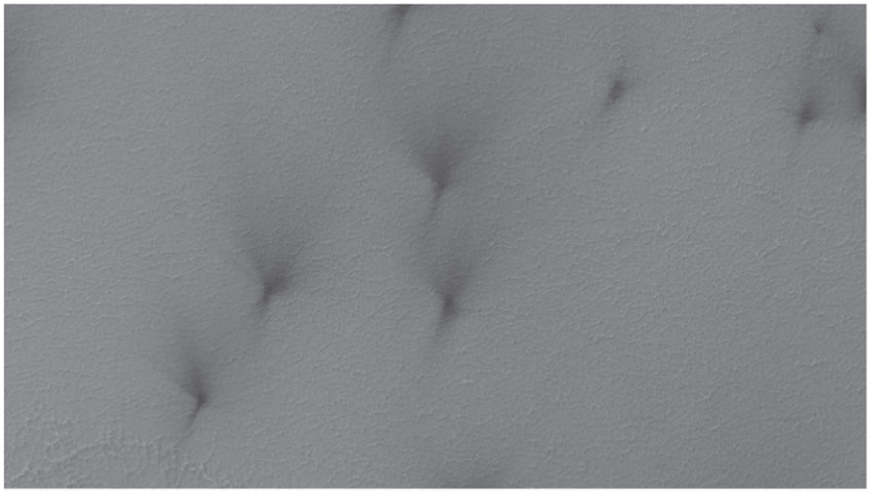

Figure 2. More than one fan can emerge from a single rupture, with the direction of each fan deposit likely due to a different prevailing wind direction at the time of its eruption. This subframe of HiRISE image ESP_011515_0980 (81.9 °S, 4.75 °E) was acquired at $L_s \approx 188.^{\circ}56$. The scene is ∼1.1 km wide.

from obliquely angled vents in the ice slab, potentially allowing the emplacement of the fans under nearly calm wind conditions, there are several considerations that argue against this happening. First, in a single HiRISE image there can be hundreds to thousands of fans, and some fans are oriented in multiple directions from a single source (Figure 2, Thomas et al. 2011). In the example shown in Figure 2, one can see that there is a common directionality for fans from multiple vents in this field of view. To explain this alignment, multiple jets over a large surface area would need to develop exactly aligned nonvertical vents. This is extremely unlikely. Furthermore, global and mesoscale climate modeling for Mars strongly suggests that modest and stronger winds are commonplace on Mars, including in the south polar region springtime. Ubiquitous ongoing sublimation of the CO_2 seasonal ice cap at that season also helps maintain some level of wind. Second, another class of dark deposits—known as "spots" or "blotches"—occurs at the same season and region as the fans. They may be the result of vertical jets erupting during nearly calm winds. And lastly, from a perspective of the mechanical stability of crystalline materials, vertical vents (e.g., along tension cracks) seem much more likely to form in the thick ice versus significantly oblique vents.

The existence of multiple fans coming from a single source suggests that the vent opening can reseal, the gas pressure builds up again over some number of days, and then the ice ruptures again at the same weak spot. Within an image there may also be areas where jets have erupted at different times (and/or under the influence of different local prevailing winds) and thus point in different directions (Figure 3).

Dark fan lengths, widths, and shapes provide information about the conditions present when they formed. Seasonal monitoring observations reveal how these features vary throughout the springtime and over multiple Martian years and thus inform us about Martian climate and seasonal processes. The first part of this paper describes the use of the lengths and orientation(s) of the fans to infer the wind speeds and directions during the spring season (assuming that the fans are due to wind acting upon nearly vertical erupting jets) for a number of monitoring sites, called regions of interest (ROIs). The 27 ROI locations around the southern polar region are plotted in Figure 4 and listed in Table 1. To carry out this

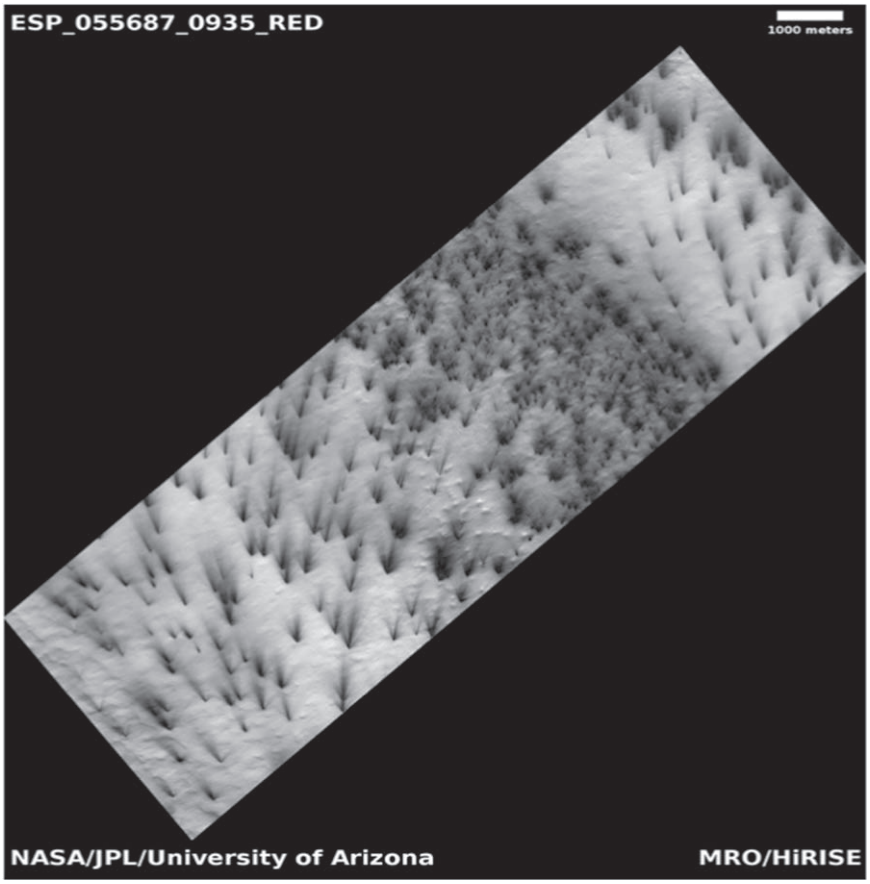

Figure 3. Multiple fan sources in this image show three different discrete fan directions—i.e., there are at least three different episodes of eruptions apparent in this map-projected image. HiRISE image ESP_055687_0935 (86.4 °S, 98.96 °E), acquired at $L_s \approx 192.^{\circ}65$ in an ROI known informally as Manhattan Classic. Some fans point north, while others have more of a northwest orientation.

investigation, we examined the fan catalog created by the Planet Four (P4) citizen science project for two Mars years: MY29 and MY30 (Aye et al. 2019). Note that the most robust inference from the P4 data set is of wind direction, as it involves fewer assumptions.

The second portion of this paper describes the synergistic analysis/comparison of seasonally resolved mesoscale climate model output and P4-derived wind velocities. We used the Mars Regional Atmospheric Modeling System (MRAMS; see Rafkin & Michaels 2019 and Section 6.1) to estimate high-resolution near-surface wind speeds and directions over the entire south polar region for multiple seasonal windows. The modeled wind directions were compared to the P4-derived wind directions in order to partially validate and to gain confidence in the model output (wind speeds were also later compared). Additional three-dimensional atmospheric context from the model output was used to better understand how and at what time of day the fans may have formed.

2. Planet Four (P4) Fan Catalog

This work utilizes the catalog of seasonal fans identified in HiRISE imagery by the online P4 citizen science project over several locales in the south polar region (mapped in Figure 4) during MY29 and MY30 (Aye et al. 2019) spring seasons with L_s ranging from 170° to 280°. P4 recruits the general public to participate in mapping the shapes, sizes, and directions of the dark seasonal deposits visible in HiRISE images in the southern spring and summer. The reader is referred to Aye et al. (2019) for a detailed description of the P4 project and the generation and validation of the first catalog of seasonal fan markings. We provide a brief overview of the project and catalog generation below.

HiRISE color images (with ∼30 cm pixel^{-1} resolution) of the monitored ROIs are divided into smaller overlapping subimages that are reviewed by multiple volunteers on the P4 website. Their independent assessments are combined to identify seasonal deposits in the HiRISE subimages. The volunteers are tasked with marking seasonal deposits (if there are any visible) in the image presented on the P4 online classification interface. For this task, volunteers are provided with two drawing tools in the web interface:

1. The "blotch" tool—an ellipse to mark deposits that show no clear directionality.
2. The "fan" tool—a triangle with a rounded base to mark those deposits that are fan shaped.

A bespoke clustering algorithm is employed to take the output from the web interface and combine all the volunteer markings from each HiRISE subimage to outline the seasonal deposits and identify whether the features are blotches or fans. At times, distinguishing between blotches and fans is not easy, for example, in cases where it is hard to see the starting point of a fan. Thus, the blotch catalog might have some features that might be better categorized as fans, but we chose to neglect these. For this work, we focus on the P4 fan catalog, composed

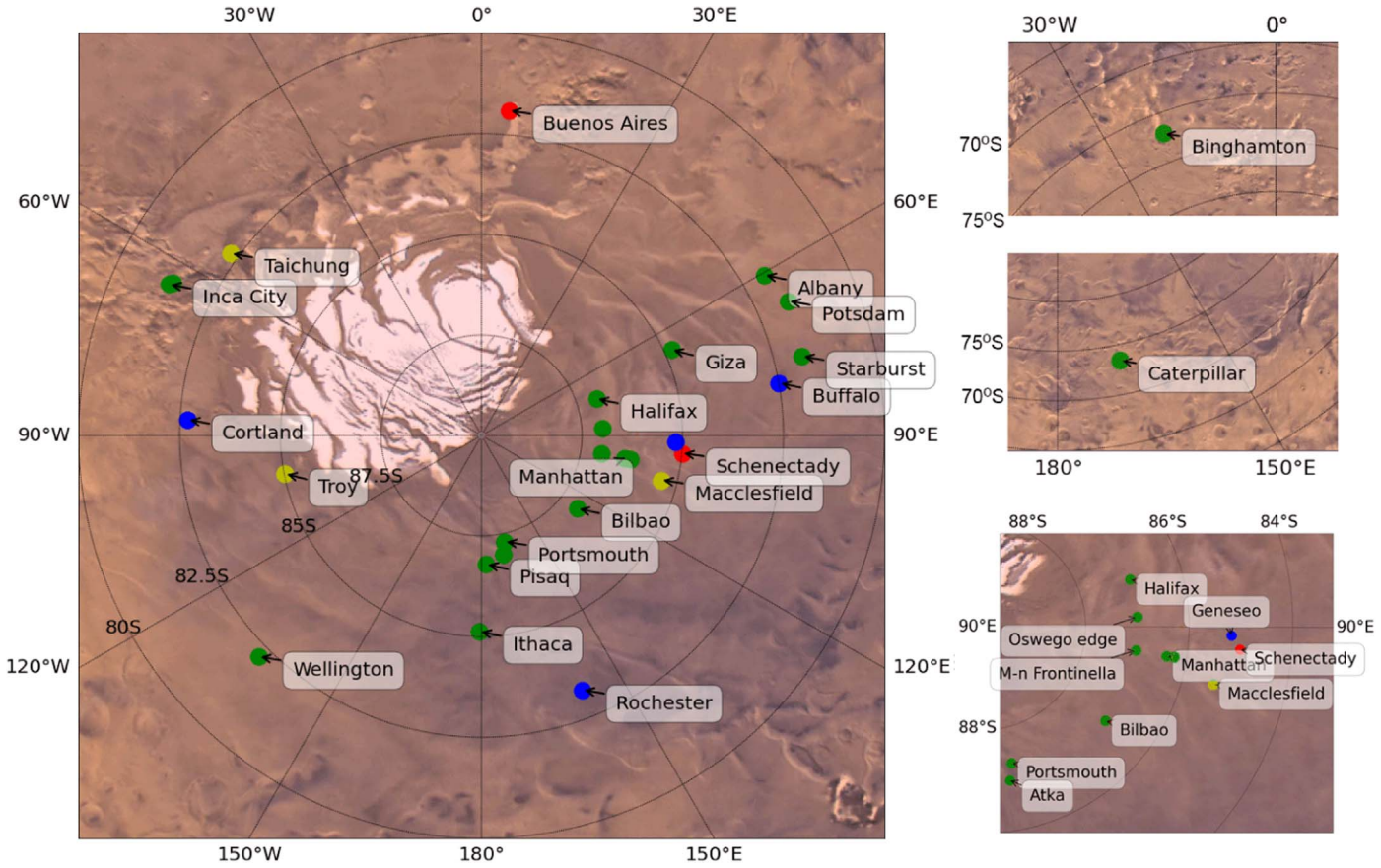

Figure 4. Locations of ROIs monitored by HiRISE and studied in this paper. ROI positions are marked with circles color-coded to indicate a qualitative goodness of fit between P4-derived wind directions and MRAMS-simulated wind directions for the same ROI and time: red = poor or no fit; green = good fit; yellow = partial fit; blue = undetermined (due to lack of observations). The two top right panels show ROIs that are located outside the primary polar area plotted on the left. The bottom right panel shows additional detail of the dense region between longitudes 60 °E and 180 °E.

of 158,476 seasonal deposits where 50% or more of the volunteers who marked each feature classified it as a fan with clear directionality and a visible starting point. Each fan object inside the catalog possesses a set of descriptors: location inside the P4 frame and original HiRISE image, latitude and longitude location, spread angle, alignment angle, and length. In this work we mainly make use of a fan's alignment angle and length, as well as its global association with one of the ROIs (location lat/lon), and time at which the original HiRISE image was taken. We do not make use of spread angle, which potentially carries information about either wind speed (the faster winds are, the narrower fans are expected to be) or eruption duration (assuming that the wind direction shifts over time). These effects will be addressed in future work.

3. Methodology

In this section we describe how we determine wind directions and estimate wind speeds from the P4 fan catalog. Throughout this section we use one ROI named Giza as an example for the methods applied. We selected Giza because the number of fans here is consistently high and variations of most statistical values are smooth, which makes it easier to understand (and describe) the concepts behind our methods. The constancy of seasonal fan behavior in Giza is largely due to its location on a relatively gentle equator-facing slope without extreme topographical obstacles nearby.

It has been hypothesized that fans are created during jet eruptions under the influence of wind (Thomas et al. 2010). Thus, by studying fan deposits, we will be making conclusions about the winds both at the time of jet eruption and in the layer of atmosphere where the eruption occurs. The material from the vent is assumed to be expelled nearly vertically into the atmosphere, where it is deflected by the wind and thus forms fan-shaped deposits toward the downwind direction (Thomas et al. 2010). The amount of time that a particle spends in the vertical flow of the jet, i.e., from the moment it passes through the vent to the maximum altitude it achieves, is a matter of seconds. This is different from the overall jet eruption duration, which in the Kieffer model scenario depends on the volume of the trapped CO_2 gas reservoir that is being emptied, the vent size, and the pressure accumulated below the ice slab before the eruption. The greatest altitude to which the material is propelled determines the altitude of the winds that can be measured. We expect this to be limited to the lowest reaches of the atmosphere—up to an altitude of ∼200 m—because models of jet eruptions indicate that the heights of steady-state jets reach no more than 100 m, and although eruptive transient jets are not adequately studied yet, they are not expected to exceed this height by more than a factor of two (Thomas et al. 2010). The faster the wind, the farther away from the vent the material is deflected and the longer the fans will be. The speed of the wind during the eruption can thus be estimated from the length of the fan-shaped deposits.

Table 1
Coordinates (Longitude and Areocentric Latitude) of ROIs Studied in This Work, Where Fan Observations Were Used to Estimate Wind Speeds and Directions

Location (ROI)	Latitude, °N	Longitude, °E
Albany	−81.93	60.4
Atka	−86.98	169.7
Bilbao	−87	127.3
Binghamton	−73.53	339.5
Buenos Aires	−81.9	4.8
Buffalo	−82.5	80
Caterpillar	−74.22	168.5
Cortland	−82.69	273.1
Geneseo	−85.18	92
Giza	−84.82	65.7
Halifax	−87	72.3
Inca City	−81.38	295.8
Ithaca	−85.13	180.7
Macclesfield	−85.4	103.9
Manhattan Classic	−86.39	99
Manhattan Cracks	−86.25	99
Manhattan Frontinella	−86.99	98.7
Oswego Edge	−87	86.4
Pisaq	−86.8	178
Portsmouth	−87.3	167.8
Potsdam	−81.68	66.3
Rochester	−83.2	158.4
Schenectady	−85	95
Starburst	−81.8	76.1
Taichung	−82.3	306
Troy	−85.02	259
Wellington	−82.2	225.2

Note. ROI names are informal.

P4 provides outlines of fans and thus a possibility to determine the direction and speed of the wind at the moment of jet eruptions. The P4 catalog contains outlines of up to thousands of fans per HiRISE image. In this paper we treat each HiRISE image as one data point and aim to determine temporal changes in the mean wind direction and speed over an entire HiRISE image from one L_s (seasonal) interval to the next. The possible variations of wind directions within one HiRISE image will be the focus of future work.

3.1. Fan Directions and Wind Directions

Using the P4 catalog, we create histograms of fan directions and fan lengths for each HiRISE image. A series of such histograms for ROI Giza (84.82 °S, 65.7 °E) are shown in Figure 5 (histograms for the other ROIs can be found in Appendix B, and derived P4 fan directions and lengths are in the supplementary data files). The left column shows histograms of fan directions (measured clockwise from north) for six HiRISE images acquired at L_s ranging from 185° to 227°. The right column shows histograms of fan lengths (in meters) for the same HiRISE images that are used for wind speed estimates (see Section 3.2). The bin size of these histograms varies between 1° and 10° for fan direction and between 1 and 3 m for fan length—individually determined for each HiRISE image depending on the number of fans that were detected in the image and the distribution of their directions and lengths. The scale of *Y*-axis (showing fractional number of fans) changes in accordance to bin width because the histogram is normalized so that its area is equal to 1. This normalization is required to make Weibull and Gaussian curve fitting (see more details on it below) fully automatic and thus procedurally identical for different HiRISE images that have vastly different absolute numbers of fans.

Inspecting the histograms in Figure 5, we can determine the most probable fan direction. It is equal to the position of the maximum histogram value or—as we aim to reduce the impact of statistical variations within bins—the maximum of a smooth curve fitted to the histogram shape. We use the Weibull distribution to fit the histogram's shape and quantitatively determine the position of its maximum. The Weibull distribution function has two free parameters that are being varied in the fitting procedure: the shape parameter and the scale parameter of the distribution. This allows fits of asymmetrical distributions that are common among P4 histograms of fan directions and lengths. Then, we locate the position of the maximum (or maxima if there are two) of the fitted curve. We do not use the fitting parameters themselves. The position of the maxima serves as the most probable fan direction or fan speed for the subsequent analysis. We keep the fitting procedure simple and fully automatic without any manual alteration of either starting assumptions or fitting quality. This leads to less desirable fit quality for some histograms than could potentially be achieved with manual intervention: for example, the amplitude of the maximum is often fitted poorly. However, the main focus of the fitting is to find the locations of the maxima and maintain uniformity of analysis for all ROIs at all L_s. There are, however, the special cases (e.g., as in ROI Macclesfield in Figure 6) when the histogram has two well-determined modes. In those cases, the Weibull function fails to provide a viable fit. Instead, for bimodal distributions we chose to use a combination of two Gaussian functions. Each Gaussian has two free parameters to vary (mean and standard deviation), while their combination has also to account for the ratio of the two maximums. In either case, Weibull or double Gaussian, the aim is to determine the position of the maximum (or maxima) that determines the most probable fan direction (or length) for a given histogram. We can then plot the most probable fan direction versus L_s, as shown in the bottom panel of Figure 7.

As evident from Figures 5 and 6, the location of the peak of the fan direction histograms changes. In the case of Giza (Figure 5), it shifts clockwise with season (L_s). This can be interpreted as being due to the shift in wind directions during jet eruptions that happened between these HiRISE observations. It is surprising how marked the shifts are between $L_s \approx 185°$ and $L_s \approx 200°$ and between $L_s \approx 203°$ and $L_s \approx 221°$. One would expect that the fan deposits created during the early eruptions at $L_s \approx 185°$ would still be visible at $L_s \approx 200°$. This is partially true: the histogram at $L_s \approx 200°$ is wider than at $L_s \approx 185°$, which means that it includes the fans from previous eruptions. However, the newly created fans are so much more numerous that they dominate the histogram, shifting its maximum toward the north. The shift between $L_s \approx 203°$ and $L_s \approx 221°$ is even more pronounced: here the histogram becomes narrower at $L_s \approx 221°$, which means that the fans from the previous image are no longer (easily) visible.

We can estimate histogram widths at FWHM either directly from histograms or mathematically from fitted Weibull curves. The histogram widths vary: the histogram at $L_s \approx 185°$ is the narrowest, and that at $L_s \approx 200°$ is the widest. The widths of the P4-derived wind direction histograms are not due to

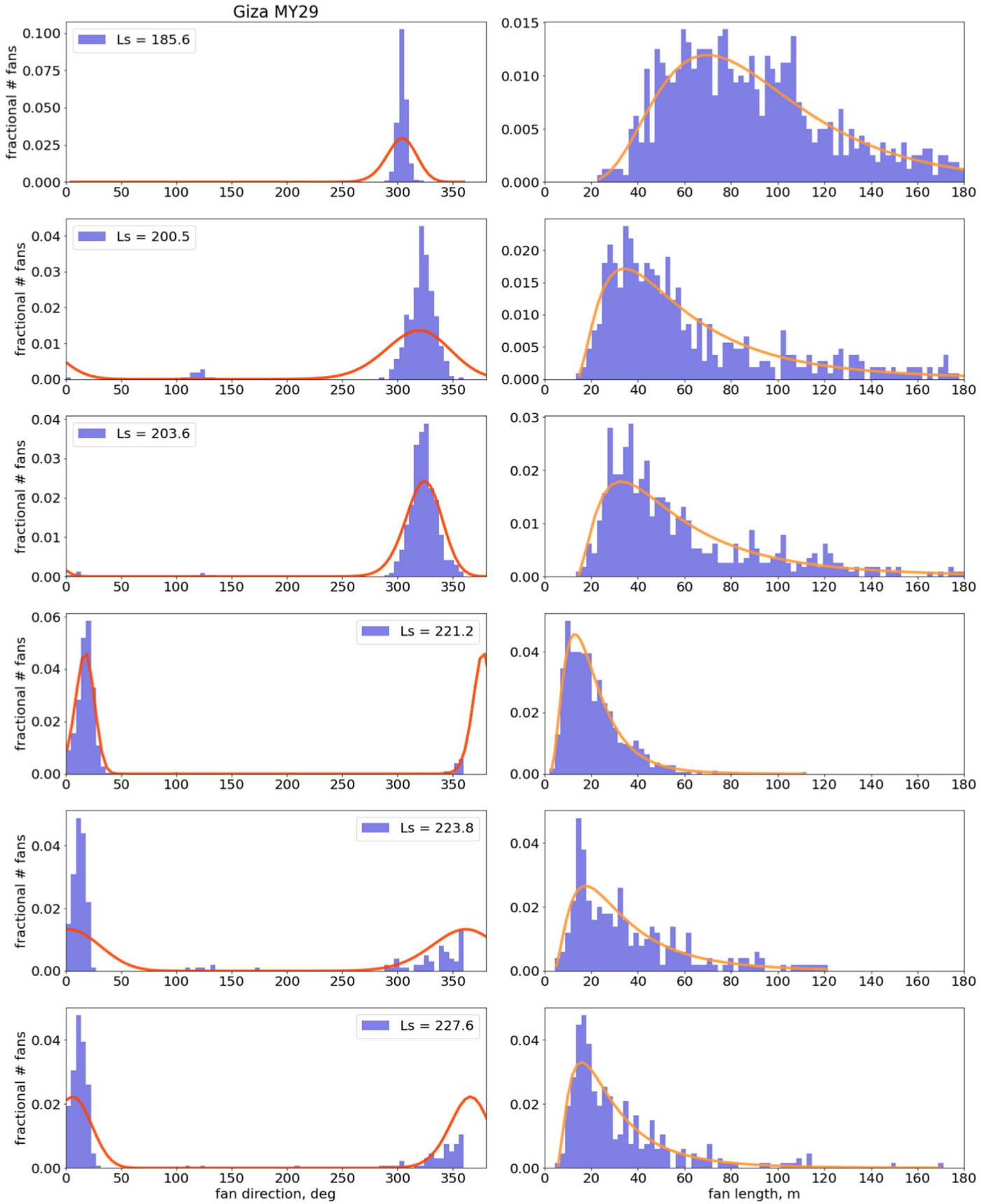

Figure 5. Histograms (blue) showing normalized distributions of P4-derived fan directions (left panels; best-fit Gaussian curves are shown) and fan lengths (right panels; best-fit Weibull function curves are shown) at ROI Giza (84.8 °S, 65.7 °E) for six HiRISE images acquired from L_s 185° to 228° (top to bottom). *Y*-axis shows fractional number of fans normalized in the way that the area under the histogram integrates to 1.

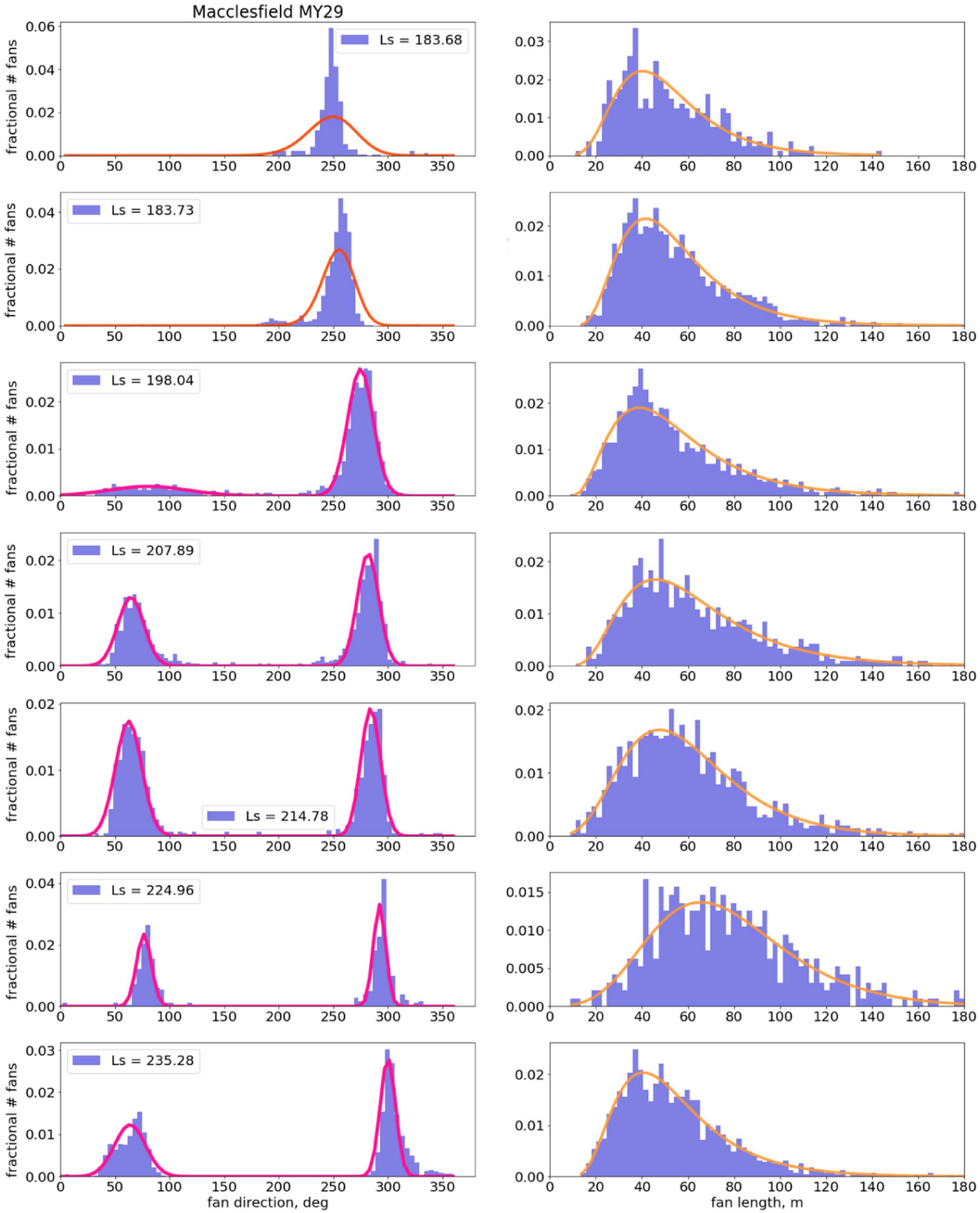

Figure 6. Distributions of P4-derived fan directions (left; best-fit Gaussian curves are shown) and lengths (right; best-fit Weibull function curves are shown) at ROI Macclesfield (data visualization similar to Figure 5). Fan direction distributions in this ROI in MY29 at $L_s \approx 198°$–$235°$ show two clear peaks (i.e., a bimodal distribution) pointing to the appearance of a second mode in the wind directions. Magenta curves represent best fits of two Gaussian curves to the wind direction histograms.

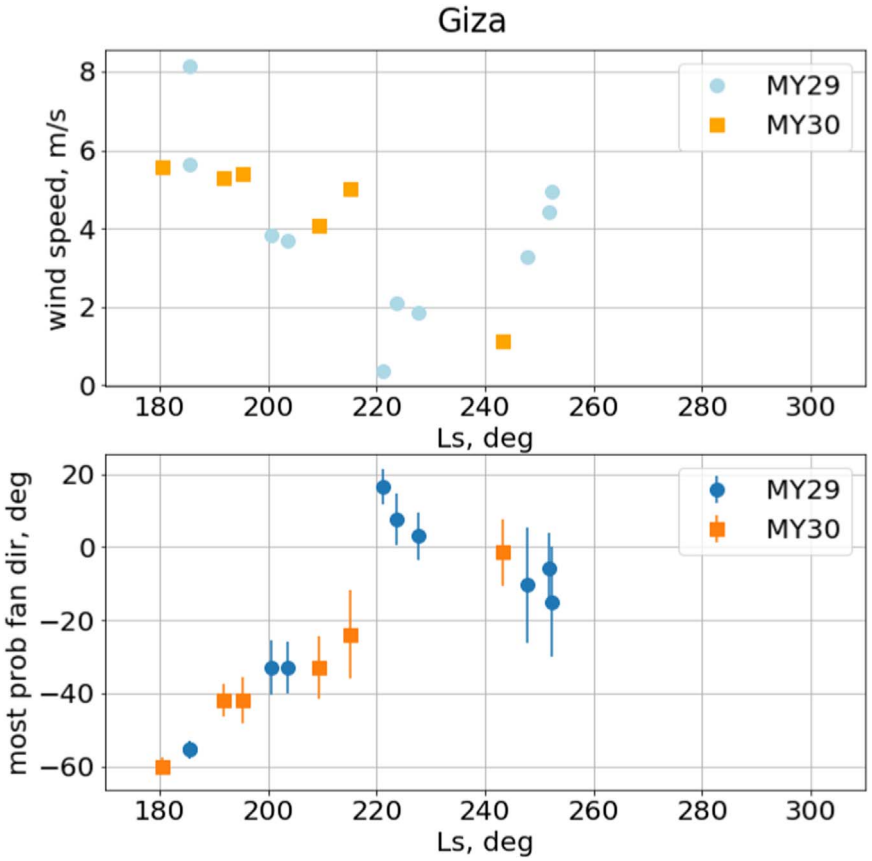

Figure 7. Prevailing P4-derived wind speeds (top panel) and directions (bottom panel) vs. L_s during local spring are compared for MY29 and MY30 at ROI Giza. To visualize the width of the wind direction histograms, we use error bars in the bottom panel. They should serve as a measure of the variability of P4 markings over a single HiRISE image, and they do not provide a quality evaluation for the measurement made (i.e., they are not actual error bars).

inaccuracies in the citizen scientists' measurements. No single correct direction of fans for the HiRISE image can be assigned from P4 data because fan directions differ throughout each image owing to local natural variations in topography and atmospheric conditions at the time of their eruption. In fact, each value entry in the histograms already has its own measurement error. The width of each of these histograms tells us about the physical properties of the distribution of fans, which often (but not always) can be extended to the distribution of winds. For example, a relatively flat distribution with a very wide histogram means that there was no consistent prevailing wind during eruptions of the jets—i.e., the eruption-time winds were constantly changing, the eruption times of day were significantly variable, and/or we are looking at the integrated record of multiple jet eruptions over an extended period of time that all got preserved. Another possibility at some sites is that the wind direction is strongly influenced by local topography and varies considerably in different parts of the area covered by the HiRISE image. As we noted above, this is not the case in Giza, nor is it for the majority of our ROIs, with possible exceptions being ROI Inca City and late spring at ROI Oswego Edge (see Section 6). In contrast, if the histogram shows a narrow well-defined peak, it means that the wind direction during jet eruptions was very stable (and possibly also that the eruption time of day is nearly constant).

In order to visualize the variability of P4 fan directions and lengths, we plotted the FWHM of the histogram at each L_s as an "error bar" (e.g., as in Figure 7). We remind the reader that these are only intended to convey a measure of the variability of P4 markings over each HiRISE image (and, by extension, the variability of the wind and/or eruption time of day) and not to indicate actual error bars (i.e., some kind of measurement quality metric).

The last detail about understanding P4 histograms is a warning about the integrated effect of the seasonal history of surface changes. The very first image in each ROI is acquired when the surface is fresh after the winter deposition of CO_2 ice. Very little dusty jet activity has happened yet, and thus we can treat the values derived from these first images as uncontaminated. The subsequent images tell a different and more complex story because the activity that is observed in the previous images inevitably leaves marks that can be observed later. We often do not have the means to differentiate how much of the previous fan markings are still visible in later images unless the statistics change dramatically (allowing us to neglect this effect). This is what happens in Giza between $L_s \approx 180^\circ$ and $L_s \approx 230^\circ$: the fan directions and sizes constantly change, which means that new fans are being deposited. This is usually the case for most of the ROIs; however, in some it is not. If there is no significant change, it might be because either new fans are exactly the same as the old ones or there are no new fans. These two situations imply two quite different seasonal process scenarios, but they cannot be differentiated using the P4 data alone—in Section 6 we will discuss how the addition of atmospheric modeling may be used to differentiate between them.

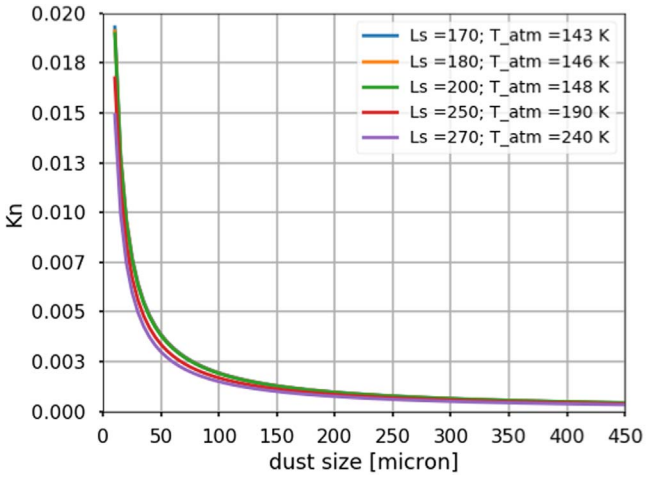

Figure 8. Knudsen number calculated for particle transport in the near-surface southern polar spring atmosphere. Temperatures are lower-atmospheric temperatures derived from the MCD for the corresponding L_s.

Note that all of the above discussions in this section concerning histograms of wind direction can also be applied to histograms of fan lengths.

3.2. Inferred Wind Speed Derivation

Using measurements of fan lengths from the P4 catalog, we aim to estimate wind speeds during the jet eruptions. Unlike the wind directions, which can be directly determined from fan directions, wind speed estimates require a more complex approach. We need to consider the state of the Martian atmosphere, physical properties of the materials involved, and the physics behind the jet eruptions. First, we need to determine whether in our problem the flow of the Martian atmosphere around a dust particle can be considered to be a continuum flow. The standard is to use the Knudsen number to evaluate whether the particle is in a continuous flow regime, molecular flow, or a mixture of the two. The Knudsen number indicates how rarefied the flow it describes is. Values of K_n less than 0.01 indicate continuous flow; values between 0.01 and 10, transitional flow; and values greater than 10, molecular flow. The Knudsen number depends on the state of the Martian atmosphere and a representative physical length scale of the problem (in our case, dust particle size):

$$K_n = \frac{\lambda}{r_p}, \quad \lambda = \frac{2\eta}{\rho_{\rm atm} V_{\rm atm}}. \tag{1}$$

Here λ is the mean free path of CO_2 gas in the atmospheric layer under consideration, r_p is the dust particle radius, η is the dynamic viscosity of CO_2 measured at the atmospheric temperature, $\rho_{\rm atm}$ is the mass density of the atmospheric gas, and $V_{\rm atm}$ is the atmospheric gas molecular velocity.

We next consider dust and sand-sized particles gravitationally setting out of the polar spring atmosphere. The particle size distribution of such a mix is discussed in Section 3.2.1. We can estimate the relevant range of K_n during the south polar cold jet eruption season by obtaining selected atmospheric state variables (temperature, pressure, air density) from the Mars Climate Database (MCD, derived from Mars global climate model output; http://www-mars.lmd.jussieu.fr/mars/access.html) for a range of L_s and P4 ROI locations.

We need to consider the atmospheric layers closest to the surface (up to ~200 m because that is the maximum height jets are able to penetrate upward; Thomas et al. 2010) and their minimum temperatures, because K_n is inversely related to T, and we are interested in the maximum values for K_n. Figure 8 shows that Knudsen number depends weakly on the atmospheric state and much more strongly on particle size. If we consider a commonly used limit for continuous flow ($K_n < 0.01$), then particles larger than 20 μm can be considered to remain in the continuous flow regime. For smaller particles we must additionally account for Cunningham slip-flow correction, allowing consideration of particle movement in the mixed regime (between molecular and continuous regimes).

The terminal velocity of particles falling through the atmosphere is determined by the gravity of Mars and the viscosity of the dominantly CO_2 atmosphere. Applying Stokes's law,

$$\frac{4}{3}\,\pi\, r_p^3\, \rho_p\, g = 6\,\pi\, r_p\, \eta\, V_{\rm fall}, \tag{2}$$

where r_p is again the particle radius, ρ_p is its mass density, g is the gravitational acceleration, and $V_{\rm fall}$ is the terminal velocity of the particle. Thus, after accounting for the Cunningham slip-flow correction (Cunningham 1910; Schmid et al. 2002), terminal velocity is

$$V_{\rm fall} = \frac{2\rho_p\, g\, r_p^2}{9\,\eta}(1 + \alpha K_n),$$
$$\alpha = 1.246 + 0.42\exp\left(\frac{-0.87}{K_n}\right). \tag{3}$$

The most probable atmospheric gas molecular velocity is

$$V_{\rm atm,mp} = \sqrt{\frac{2\,k_{\rm B}\,T_{\rm atm}}{M_{\rm atm}}}, \tag{4}$$

where $k_{\rm B}$ is the Boltzmann constant, $T_{\rm atm}$ is the temperature of the atmospheric layer under consideration, and $M_{\rm atm}$ is the molar mass of the atmospheric gas. We set the upward air advection velocity to zero and neglect the turbulence of the atmosphere—advection and turbulence both decrease sedimentation velocity. Thus, we calculate an upper limit on gravitational sedimentation velocity, which will eventually yield a lower limit on the wind speed.

We can now estimate $V_{\rm fall}$—the terminal velocity of the particle—depending on its size. We assume that each mineral particle is entrained by the general atmospheric flow immediately after reaching the maximum height to which particles can be brought up by the jets (i.e., after its vertically oriented momentum becomes insignificant). Due to our assumptions, vertically it is influenced only by gravity and small-scale atmospheric drag, and horizontally it moves with the wind. Therefore, if we know the maximum height to which particles can be brought up by the jet ($H_{\rm jet}$) and the length of the resulting surface deposit ($L_{\rm fan}$) and ignore horizontal drag effects, the calculation of the inferred wind speed ($S_{\rm wind}$) becomes straightforward:

$$S_{\rm wind} = \frac{L_{\rm fan}\, V_{\rm fall}}{H_{\rm jet}}. \tag{5}$$

The length of the fans is obtained from the P4 catalog, the terminal velocity of the particles that were propelled up by the CO_2 jet depends on the size and composition of the particles (see Section 3.2.1), and the assumed height of the jet is discussed in Section 3.2.2.

3.2.1. Particle Size Distribution

We consider that the under-ice gas flow that feeds the CO_2 jets mobilizes part of the top layer of the permanent substrate together with any dust that was deposited during the previous summer. This means that the size distribution of solid material in the jet must have a shape similar to that of the typical south polar substrate (perhaps similar to the particle size composition determined for the Phoenix landing site; Pike et al. 2011).

When brought into the atmosphere by the jet eruption, smaller particles will sediment more slowly, resulting in greater atmospheric residence times (estimated at more than 6 Mars hours for 20 μm particles) and thus have a greater susceptibility to atmospheric transport processes. Due to this, the finer dust is deposited relatively uniformly over large areas. It still contributes to the general darkening of the seasonal ice surface and can be detected in the fan deposits, but it is not the material that primarily forms the albedo feature that P4 citizen scientists recognize as fans. Therefore, we will not consider particles smaller than 20 μm for the wind speed calculations. This size limit coincides with the transition from the molecular to continuous flow regime discussed above.

Some additional information for the particle sizes in the seasonal deposits can be found in Piqueux & Christensen (2008). Taking the albedo and observed surface temperature of fan deposits into account (compared with "non-fan" CO_2 ice), thermal modeling predicts that the deposits could be composed of either a 0.5 mm layer of 2 μm, 1 mm of 10 μm, or 5 mm of 150 μm mineral particles, respectively. Kieffer (2007) furthermore determined that a 1 mm thick layer best fits thermal modeling results, while 100 μm particles best explain the observed shape of the fan deposits. If not stated otherwise, in this paper we will use a default monodisperse particle size of 100 μm.

3.2.2. Jet Height

According to Section 5, wind speed is proportional to the ratio of fan length to jet height. Fan length can be derived from P4 data, and CO_2 jet height can be estimated via modeling of the jet eruption. Thomas et al. (2011) found that in the simplest case of steady-state outgassing through a vent, the maximum height that the Martian jets can reach is about 100 m. This is not the absolute maximum because the transient eruption case was not considered and it should have a larger eruptive potential and consequently a greater jet vertical extent. However, for the purpose of our work the steady-state solution appears to be the more appropriate one: P4 observes a large number of fans predominantly oriented in the same direction (Aye et al. 2019). This could be interpreted as follows: the jets that created the fans were erupting during the same wind conditions, i.e., simultaneously or quasi-simultaneously. A large number of transient eruptions that happen simultaneously is less probable than steady-state outgassing from multiple simultaneous vents. We consider the maximum jet height to be $\sim$100 m for the purpose of this paper. The jets can be smaller than that, of course. In such a case of a shorter jet, the wind speeds must be proportionately greater to result in a given fan length. For example, for the Manhattan ROI at $L_s \approx 200°$, the mean fan length is 70 m. If we assume that the jets that create these fans are 100 m tall, the derived wind speeds for dust particle sizes < 300 μm are all below 15 m s^{-1}. However, if the jets are shorter, e.g., 20 m tall, it would require a wind speed in the range of 50 m s^{-1} to create 70 m fan lengths. Thus, since we assume that the steady-state jets are $\sim$100 m tall, our P4-derived wind speed results are actually estimates near the lower wind speed limit for fan creation.

4. P4 Data Limitations

With the methods described above, our P4 results provide wind directions and speeds limited to the lowest reaches of the atmosphere because, according to Thomas et al. (2011), CO_2 jets are not expected to reach above 100 m. HiRISE observations that show fans are also limited to a specific season: between the end of the southern polar night at around $L_s \approx 170°$ and complete sublimation of the seasonal frost at about $L_s \approx 260°$, depending on the location. In addition, there is a cumulative effect of deposits from younger jets overlaying the material erupted from jets active earlier. This could potentially cloud our understanding of the exact timing of the winds measured by P4 during the later part of the relevant L_s range. Luckily, as will be shown in Section 6, at several ROIs the wind direction shifts considerably between HiRISE observations. As evident from histograms of wind directions at these ROIs (e.g., Figure 5), we do not observe a significant lag in the P4 data for fan directions. From one L_s to the next, the histogram maximum shifts significantly, indicating that new deposits are oriented at a considerably different angle from before. If there are any fans left from the previously imaged L_s, they are a statistically small part of the population of fans in each image. This data property allows for the time-dependent wind direction and speed estimates at those ROIs. Moreover, this continual fading and fresh emplacement behavior of the fans may similarly occur at other ROIs that do not exhibit much seasonal fan direction change. We have no observational evidence that the time continuity of the fan emplacement process is drastically different between ROIs. Although it is likely a gradual (and continual) process, the details of fan fading are poorly known and will be further investigated in future work. Thus, here we assume that at all ROIs, fading is fast enough compared to the fan emplacement timescale to unambiguously reflect intraseasonal wind direction and speed changes in HiRISE imagery.

While wind directions are derived directly from P4 fan direction distributions, wind speeds have a much larger uncertainty due to all the assumptions that were made for their calculation (Section 3). Therefore, we are more confident in the wind directions than the wind speeds. Consequently, in Section 6 below, when we consider goodness of fit between the MRAMS model output and P4 data, we place a greater weighting on the wind direction comparison.

5. Mesoscale Climate Model Description

MRAMS (first described in Rafkin et al. 2001, with further updates in Michaels & Rafkin 2008; Rafkin & Michaels 2019) is a nonhydrostatic, fully compressible, limited domain (i.e., not global) atmospheric model that uses nested grids to estimate/predict atmospheric conditions on Mars at higher

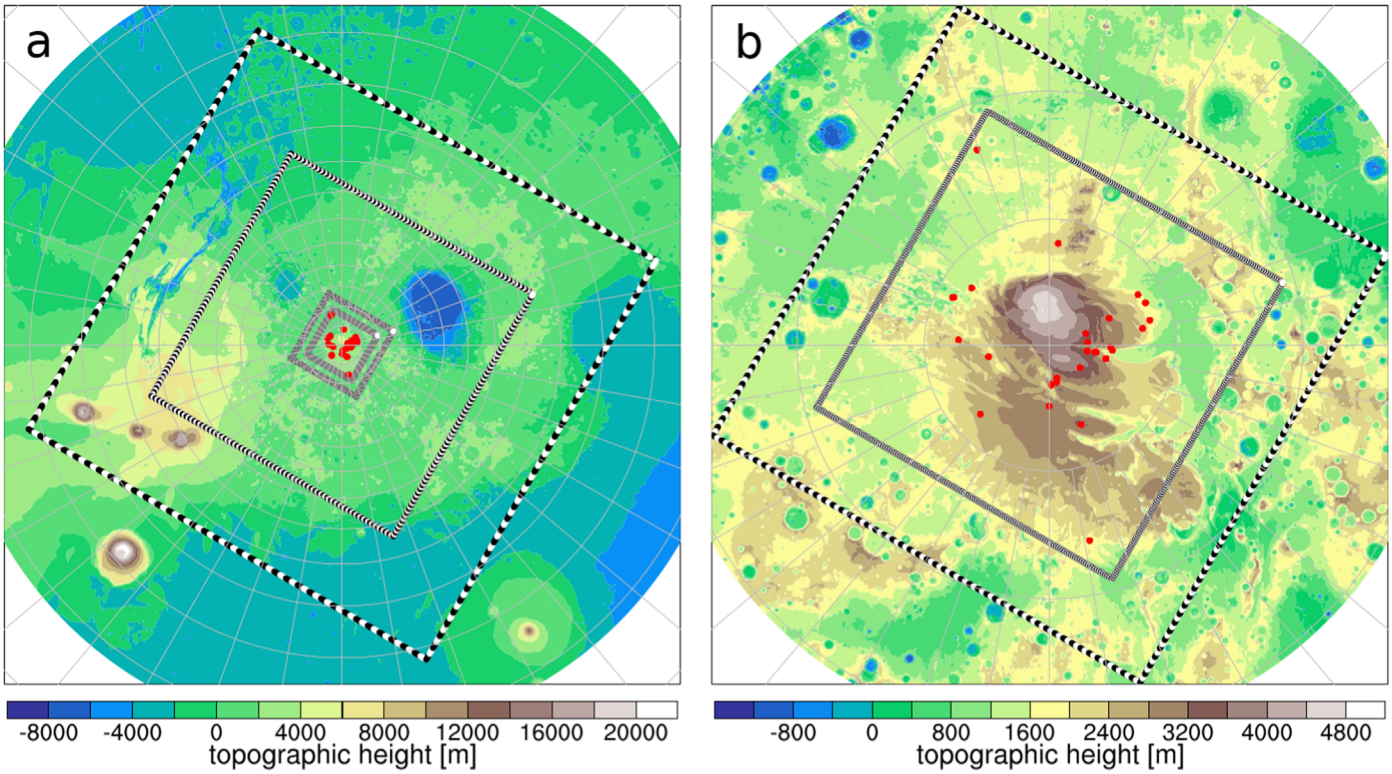

Figure 9. Geographic overview of the four MRAMS telescoping grids (square boxes) used for this work, overlaid on colorized MOLA topography. Red circles indicate P4 ROI locations, longitude = 0° is up, and latitude and longitude lines are shown every 10°. (a) The outermost (and coarsest) grid 1 is where the time-dependent GCM boundary conditions are applied, grid 2 resolves the key large-scale regional topographic features relevant to the south polar area, and grids 3 and 4 are near the center. (b) Grid 3 is an intermediate grid needed to gradually step down the model spatial resolution to the target grid spacing of < 5.8 km on grid 4 (278 × 278 horizontal points), which contains all P4 ROIs.

spatial resolutions. MRAMS includes topographic shadowing and slope effects, a state-of-the-art radiative transfer scheme for Mars, boundary layer turbulence parameterizations, surface characteristics and topography from gridded spacecraft data sets, and a multilevel subsurface thermal model (including CO_2 ice properties and evolution). MRAMS output has been successfully utilized before to further interpret spacecraft observations of both aeolian and cloud features (e.g., Rafkin et al. 2002; Rafkin & Michaels 2003; Michaels et al. 2006; Chojnacki et al. 2011).

Traditional lower-resolution (e.g., grid spacing >100 km) global climate models cannot properly represent the effects of complex terrain with relatively high relief (like that in the south polar region) on the atmosphere. However, higher-resolution climate modeling can better represent such terrain and can thus provide insight into the direction and ability of winds on smaller spatial scales to move sediment and transport dust, along with its timing (both time of day and seasonal).

The model is easily configured over a wide range of user-specified regions and horizontal grid spacings (can range from meters to hundreds of kilometers). The vertical grid typically consists of 60 or more layers that use an altitude-based terrain-influenced coordinate system, ranging in thickness from meters or a few tens of meters near the surface to a few kilometers at the model top (at a height of 50–100 km). A nearly unlimited number of multiple-nested, two-way interactive grids may be used in a simulation, allowing the model to resolve small-scale phenomena embedded in larger-scale systems.

MRAMS is not a Mars global climate model (MGCM). It has regional, not global, coverage, and it is designed to run over relatively short time periods (e.g., five Mars days). MRAMS therefore requires the user to supply initial conditions and time-dependent boundary conditions, which are routinely obtained from an MGCM solution—we utilize recent NASA Ames Research Center MGCM (Haberle et al. 1993, 2019) simulations for these purposes. The time-dependent boundary conditions are needed in order to capture important large-scale atmospheric phenomena (e.g., atmospheric tides induced by solar heating) that may propagate into and out of the MRAMS domain. MRAMS and the MGCM both use latitudinally and seasonally varying atmospheric dust loadings based on MGS Thermal Emission Spectrometer (TES; Christensen et al. 2001) dust opacity observations (e.g., Smith 2004). MRAMS bases its terrain and surface characteristics on $1/128°$ gridded MGS Mars Orbiter Laser Altimeter (MOLA) topography (Smith et al. 2001), $1/20°$ gridded MGS TES albedo (Putzig & Mellon 2007), and $1/20°$ gridded MGS TES-based nighttime thermal inertia (Putzig & Mellon 2007).

5.1. MRAMS Simulation Configuration

The MRAMS simulations discussed here were configured with telescoping south polar stereographic grids (see Figure 9) in order to consistently characterize the atmosphere across the entire circumpolar region poleward of 70 °S at higher resolution, while still being computationally practical. The annulus between ∼70 °S and ∼77 °S was covered by a grid spacing of <20 km (the third telescoping grid), while latitudes poleward of ∼77 °S (poleward of ∼71 °S in some areas, due to the grid's noncircular shape) had a grid spacing of <5.8 km. Note that the grid spacing on each grid decreases radially away

from the south pole owing to the map projection used. The vertical grid consisted of 70 layers, ranging in thickness from ~5 m near the surface to ~2 km at the top (at a height of ~60 km). Within the lowest 100 m from the ground, the model configuration had seven vertical layers.

MRAMS was run at each of seven seasons ($L_s = 180°$, 190°, 200°, 210°, 220°, 230°, 240°), encompassing most of the time of year that fans were observed to be active. Each seasonal run was centered near the nominal midpoint of each L_s window and was 4.5 sols in duration, with the first 1.5 sols assumed to be spin-up (based on the time primary model output fields took to settle into a more repeatable pattern at large spatial scales). Thus, the final 3 sols of MRAMS output (per seasonal window) were analyzed. The model state was output with a frequency of 10 Mars minutes. For computational expediency, no cloud parameterizations were used, although we recognize that some water-ice clouds are observed to be present in this region and at this season. Atmospheric dust loading for the radiative transfer calculations was set to an MY24 scenario (i.e., including no large dust storms). Dynamic CO_2 ice evolution was permitted.

A time- and spatially dependent effective surface roughness length was used to take into account both the microscale aerodynamic surface roughness (i.e., that due to rocks, sand, and local surface undulations) and the drag on the wind exerted by the magnitude and orientation of sub-grid-scale topography (e.g., dunes, yardangs, gullies, craters; depending on the model grid spacing). Until relatively recently, MRAMS (and many other Mars atmospheric models) would typically use a nearly constant effective surface roughness length of order 1 cm (although often a smaller value over ice) and would explicitly neglect the effect of sub-grid-scale topographic drag. Landed missions and the work of Hébrard et al. (2012) strongly suggest that the microscale aerodynamic surface roughness length is significantly less than ~1 cm over much of the planet. Thus, the continued use of such a large value amounts to the implicit inclusion of a spatially variable sub-grid-scale topographic drag, but in a way that is not consistent with the actual topography. In order to better include the effects of sub-grid-scale topographic drag, the technique of Georgelin et al. (1994; itself largely based on Mason 1991) was implemented to calculate the effective surface roughness length using 1/128° MOLA topography and the global microscale aerodynamic surface roughness length map of Hébrard et al. (2012). Note that sub-grid-scale topography drag metrics are a function of wind direction, so the effective surface roughness length at each horizontal grid point is recalculated every time step.

6. Analysis and Results

In this section we present our approach to comparing P4-derived wind speeds and directions to the MRAMS atmospheric modeling results. This task includes several complications. First, we are comparing data from a relatively short event (CO_2 jet eruption and fan formation, taking on the order of minutes) that happened at some point in time before a given HiRISE image was acquired, with a constantly evolving wind field—at seasonal windows that are 10° of L_s, or ~20 sols, in duration. The MRAMS results indicate that while some of the ROIs provide more temporally stable wind conditions than others, in all of them winds vary with time of day and season (L_s). The volatility of winds in each ROI largely depends on its location with respect to the large-scale topography (south polar layered deposits (SPLD) scarps, valleys, cliffs, etc.), its own small-scale topography, and the proximity to the seasonal CO_2 ice cap crocus line at each given day of the season. At the beginning of spring ($L_s = 180°$), MRAMS indicates that airflow across the region is dominated by sublimation flows and katabatic flows, which are easily influenced by topography. By $L_s \approx 240°$ the seasonal CO_2 ice cap has retreated to ~75 °S (with outliers to ~70 °S), and the modeled airflow across this region is consequently much more dynamic, with transient cap-edge circulations strongly modulating the sublimation flows. We assume that the 3 sols of MRAMS output that we have examined for each L_s window (which straddle the center of each window) reasonably represent the range of winds at each ROI during that same seasonal bin. Second, the time of day that a given fan formed at is unknown. There is a hypothesis that CO_2 jets erupt soon after the local sunrise (Portyankina et al. 2010; Hansen et al.). However, this means that for a given ROI the local time of eruption changes from around local noon at the very beginning of spring to earlier in the morning as the season progresses. This would also imply that even at the same L_s, different ROIs would have jets erupting at different times of day, as a function of latitude. For completeness, we examine all times of day in the MRAMS output while looking for fits between the modeled and P4-derived wind directions (wind speed is compared only if/where the direction fits satisfactorily; described in more detail below). We do not observe significant differences between MY29 and MY30 in P4-derived wind directions or speeds, and thus for comparison to MRAMS results we do not make any distinction between the years. Significant differences are expected if different dust scenarios are considered: a year with a large dust storm can be expected to be different in global and local atmospheric dynamics from a year without such a storm. However, this topic is outside the scope of the current investigation.

Another relevant issue is how similar the wind direction and speed are over the entire finite height of the erupting jet, assumed to be 100 m in this work (see Section 3.2.2). In particular, the instantaneous wind direction variance in that 100 m layer should be smaller than the angular width of the resulting fan. The jets erupt into a statically stable atmospheric layer, so horizontal dispersion by planetary boundary layer turbulence should be modest. Additionally, the winds between the surface and somewhere near the jet's midpoint (e.g., 41 m) are perhaps more important than those near the top of the jet, since most of the larger particles in the jet (i.e., those that fall quickly to create the fan; not dust) will likely not reach the jet's apex. The vast majority of our modeled wind directions for the 27 ROIs (e.g., Figure 10; also see Appendix B) do not change by more than 15° between 5 and 41 m (20° between 5 and 91 m) and vary by <10° at many ROIs and/or L_s. Modeled wind speeds at each point typically increase with altitude (see Appendix B for associated plots), with most increasing $<5\ m\ s^{-1}$ between 5 and 41 m ($<8\ m\ s^{-1}$ between 5 and 91 m). When the modeled wind speeds do decrease with height, it is by a modest amount (usually $<1\ m\ s^{-1}$).

Table 2 summarizes the semiqualitative overall goodness of fit between P4 data and MRAMS output (near-surface wind direction and speed) for every ROI we have investigated. Strictly quantitative goodness-of-fit metrics are impractical to use for this task owing to the substantial variability in modeled winds from one season (L_s bin) to another, from day to day, and as a function of time of day at each ROI (reflecting the underlying stochasticity of the weather). Also recall from

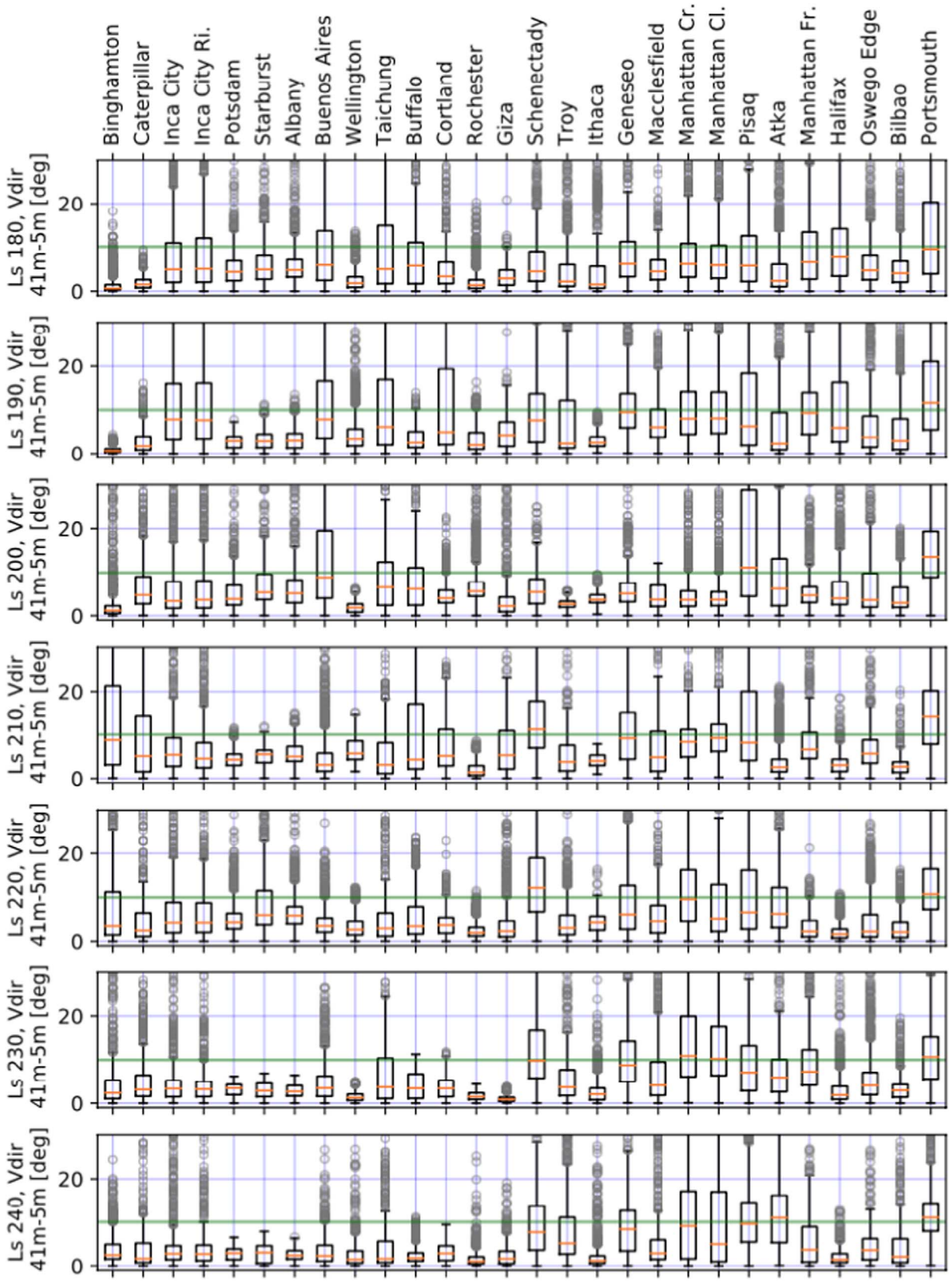

Figure 10. Statistical summary (using box/whisker plots) of the difference in modeled wind direction between ∼41 and ∼5 m for all ROIs and L_s windows (for sol 1 of each). Each box extends from the lower to upper quartiles of the data (excluding outliers, i.e., values greater than the upper quartile plus 1.5 times the interquartile range, or less than the lower quartile minus 1.5 times the interquartile range), with the median value indicated with an orange line. Whiskers extend vertically to the minimum and maximum of the nonoutlier data. Outliers (fliers) are shown as gray circles, and in some cases not all are shown owing to the *y*-axis range. The green horizontal line indicates the P4–MRAMS "good match" direction tolerance of 10°, and most of the modeled wind directions change less than that over this altitude range.

Table 2
A Comparison of Wind Inferred from P4 Data and Simulated MRAMS 5 and 91 m AGL Winds for All ROIs

ROI Name (L_s Range of P4 Data)	Sol	MRAMS 5 m Winds Compared with P4 Winds														Seasonal Direction Match (avg score)	Seasonal Speed Match (avg score)	(Latitude) Fit Category (score)
		Seasonal Bin (L_s)																
		180°		190°		200°		210°		220°		230°		240°				
		d	s	d	s	d	s	d	s	d	s	d	s	d	s			
Albany	1									=	⩾	=	>	=	>			
(221°–242°)	2									=	=	=	≳	=	≳			(81.93 °S)
	3									∼	≳	∼	∼	=	=			
	score									2	2	2	2	2	2	= (2.00)	= (2.00)	I (2.00)
Atka	1							=	⩾					∼	∼			
(212°–243°)	2							=	⩾					X	X			(86.98 °S)
	3							=	⩾					=	⩾			
	score							2	2					1	1	= (1.50)	= (1.50)	II (1.50)
Bilbao	1	X	X	X	X	X	X					=	>	=	≳			
(184°–264°)	2	=	≲	=	⩾	=	⩽					=	≳	=	>			(87.00 °S)
	3	=	≲	=	≲	X	X					=	>	=	>			
	score	2	0	2	1	1	0					2	2	2	2	= (1.80)	∼ (1.00)	II (1.53)
Binghamton	1									=	⩾							
(223°–254°)	2									=	≳							(73.53 °S)
	3									=	>							
	score									2	2					= (2.00)	= (2.00)	I (2.00)
Buenos Aires	1					=	⩽	X	X	X	X			=	⩾			
(182°–256°)	2					X	X	X	X	X	X			X	X			(81.90 °S)
	3					X	X	X	X	X	X			X	X			
	score					1	0	0	0	0	0			1	1	X (0.50)	X (0.25)	III (0.42)
Buffalo	1																	
(224°–241°)	2																	(82.50 °S)
	3																	
	score															poor P4 fan statistics		
Caterpillar	1					=	⩾											
(196°)	2					∼	≳											(74.22 °S)
	3					=	⩾											
	score					2	2									= (2.00)	= (2.00)	I (2.00)
Cortland	1																	
(183°)	2																	(82.69 °S)

Table 2
(Continued)

ROI Name (L_s Range of P4 Data)	Sol	MRAMS 5 m Winds Compared with P4 Winds														Seasonal Direction Match (avg score)	Seasonal Speed Match (avg score)	(Latitude) Fit Category (score)
		Seasonal Bin (L_s)																
		180°		190°		200°		210°		220°		230°		240°				
		d	s	d	s	d	s	d	s	d	s	d	s	d	s			
	3																	
	score															poor P4 fan statistics		
Geneseo	1																	
(278°)	2																	(85.18 °S)
	3																	
	score															poor P4 fan statistics		
Giza	1	=	⩾	=	⩾	=	≳	=	⩾	~	≳	X	X	X	X			
(185°–252°)	2	=	⩾	=	⩽	=	~	=	⩽	=	≳	X	X	=	>			(84.82 °S)
	3	=	⩾	=	⩾	=	=	=	⩽	=	≳	=	>	=	>			
	score	2	2	2	2	2	2	2	1	2	2	1	1	2	2	= (1.86)	= (1.71)	I (1.81)
Halifax	1							=	=									
(214°–242°)	2							=	≳									(87.00 °S)
	3							=	≳									
	score							2	2							= (2.00)	= (2.00)	=0pt I (2.00)
Inca City	1	=	⩾	=	⩾	=	⩾	=	⩾	=	≳	X	X	X	X			
(176°–265°)	2	=	⩾	=	⩾	=	⩾	~	~	X	X	X	X	~	≳			(81.38 °S)
	3	=	⩾	=	⩾	=	⩾	=	⩾	=	≳	=	=	=	≳			
	score	2	2	2	2	2	2	2	2	2	2	1	1	1	2	= (1.71)	= (1.86)	II (1.76)
Ithaca	1	=	⩾	=	≳	=	>	~	>					=	⩾			
(180°–252°)	2	=	⩾	=	≳	=	≳	~	>					=	⩾			(85.13 °S)
	3	=	≲	=	≳	=	≳	~	>					=	⩾			
	score	2	2	2	2	2	2	0	2					2	2	= (1.60)	= (2.00)	II (1.73)
Macclesfield	1	=	⩾	=	⩾	~	⩾	=	≳	=	≲			=	⩾			
(183°–243°)	2	~	⩾	=	⩾	~	⩾	=	≲	=	≲			=	⩾			(84.40 °S)
	3	=	⩾	=	⩾	~	⩾	~	~	X	X			~	⩾			
	score	2	2	2	2	0	2	2	1	2	0			2	2	= (1.67)	= (1.50)	II (1.61)
Manhattan	1	=	⩾	=	⩾	=	⩾	=	≲	=	⩾			=	⩾			
Classic	2	~	⩾	=	⩾	=	≲	X	X	X	X			=	≳			(86.39 °S)
(182°–281°)	3	=	~	=	⩾	=	≲	~	≲	X	X			=	≳			

Table 2
(Continued)

ROI Name (L_s Range of P4 Data)	Sol	MRAMS 5 m Winds Compared with P4 Winds														Seasonal Direction Match (avg score)	Seasonal Speed Match (avg score)	(Latitude) Fit Category (score)
		Seasonal Bin (L_s)																
		180°		190°		200°		210°		220°		230°		240°				
		d	s	d	s	d	s	d	s	d	s	d	s	d	s			
	score	2	2	2	2	2	1	1	0	1	1			2	2	= (1.67)	~ (1.33)	II (1.56)
Manhattan	1	=	⩾	=	⩾	=	⩾	=	⩽					=	⩾			
Cracks	2	~	~	=	⩾	=	⩽	=	<					=	≳			(86.25 °S)
(182°–251°)	3	=	~	=	⩾	=	⩽	=	<					=	≳			
	score	2	1	2	2	2	1	2	0					2	2	= (2.00)	~ (1.20)	II (1.73)
Manhattan	1			=	=	=	<											
Frontinella	2			=	=	=	<											(86.99 °S)
(181°–259°)	3			=	=	=	<											
	score			2	2	2	0									= (2.00)	~ (1.00)	II (1.67)
Oswego Edge	1			=	⩽	=	<					=	=	=	⩾			
(188°–261°)	2			=	⩽	=	=					=	>	=	>			(87.00 °S)
	3			=	≲	=	<					=	≳	=	≳			
	score			2	0	2	1					2	2	2	2	= (2.00)	~ (1.25)	II (1.75)
Pisaq	1							X	X					=	⩾			
(209°–235°)	2							=	⩾					=	⩾			(86.80 °S)
	3							=	⩾					=	≳			
	score							2	2					2	2	= (2.00)	= (2.00)	I (2.00)
Portsmouth	1					=	<	=	⩾	=	⩾	=	⩾	=	≳			
(200°–250°)	2					=	≲	=	≳	=	≳	=	≳	=	≳			(87.30 °S)
	3					=	≲	=	⩾	=	⩾	=	⩾	=	⩾			
	score					2	0	2	2	2	2	2	2	2	2	= (2.00)	= (1.60)	I (1.87)
Potsdam	1	=	⩽	=	⩾	=	⩾							~	>			
(181°–253°)	2	=	=	=	⩾	=	⩾							=	≳			(81.68 °S)
	3	=	=	=	⩾	=	≳							=	=			
	score	2	2	2	2	2	2							2	2	= (2.00)	= (2.00)	I (2.00)
Rochester	1																	
(222°–240°)	2																	(83.20 °S)
	3																	
	score															poor P4 fan statistics		=0pt
Schenectady	1							=	<									

Table 2
(Continued)

ROI Name (L_s Range of P4 Data)	MRAMS 5 m Winds Compared with P4 Winds														Seasonal Direction Match (avg score)	Seasonal Speed Match (avg score)	(Latitude) Fit Category (score)
	Sol	Seasonal Bin (L_s)															
		180°		190°		200°		210°		220°		230°		240°			
		d	s	d	s	d	s	d	s	d	s	d	s	d	s			
(207°)	2							∼	<									(85.00 °S)
	3							∼	<									
	score							1	0							∼ (1.00)	X (0.00)	III (0.67)
Starburst	1	=	≲	=	⩾	=	⩾	=	⩾					=	>			
(180°–267°)	2	=	≲	=	⩾	=	⩾	=	=					=	⩾			(81.80 °S)
	3	=	=	=	⩾	=	⩾	=	⩾					=	=			
	score	2	1	2	2	2	2	2	2					2	2	= (2.00)	= (1.80)	I (1.93)
Taichung	1											∼	⩾					
(227°)	2											=	⩾					(82.30 °S)
	3											∼	⩾					
	score											1	2			∼ (1.00)	= (2.00)	II (1.33)
Troy	1													∼	≳			
(181°–272°)	2													=	=			(85.02 °S)
	3													=	⩾			
	score													2	2	= (2.00)	= (2.00)	I (2.00)
Wellington	1	=	=					∼	>									
(178°–211°)	2	∼	≳					∼	>									(82.20 °S)
	3	=	≲					=	=									
	score	2	2					1	2							= (1.50)	= (2.00)	II (1.67)

Note. Topographic settings and context images for all ROIs can be found in Appendix B. ROI names are informal. Symbols in the table are used as follows: "d"—short for directions; "s"—short for speeds; "="—means a good match; "∼"—a near match; "X"—no match; "<"—most MRAMS wind speeds at/near matching wind directions are clearly less than the P4 estimates; ">"—most MRAMS wind speeds at/near matching wind directions are greater than the P4 estimates; combinations of those symbols can be used for wind speeds. Score values and goodness-of-fit category are explained in the main text.

Section 4 that the wind directions derived from measurements are significantly more robust than the P4-derived wind speeds, which involve many more assumptions. In light of the above, we decided to determine semiqualitative goodness-of-fit metrics for each ROI, which take into account all the seasonal (L_s) bins and simulated sols that we have considered. We use model output from both the 5 and 91 m (above ground level (AGL)) vertical levels for this analysis, in order to be more representative of the winds over the assumed 100 m CO_2 jet height.

The first metric indicates to what degree there are modeled MRAMS wind directions that match the P4 wind direction(s) at that ROI. The methodology we used to assess the goodness of fits is as follows:

1. For each ROI at each L_s and for each of the 3 sols of MRAMS output we first determine whether P4 and MRAMS wind directions are within 10° of each other (at any local time of day). If they are, we call this fit a "good match" for wind directions. In Table 2 this corresponds to "=" and its cell is highlighted green. If there is such a wind direction match within 20°, we call it a "near match" for wind directions ("∼"; highlighted in yellow). If there are no MRAMS wind directions within those tolerances, we call it "no match" for wind directions ("X"; highlighted in red).
2. We then proceed to determine whether, for the matching wind directions (i.e., along/near the same P4 wind direction line), the associated MRAMS wind speeds are consistent with or greater than the P4-derived wind speed (itself an estimate near the lower speed limit; see Section 3.2.2). There are two wind speed consistency thresholds: within $\pm 1\ m\ s^{-1}$ ("=") and within $\pm 3\ m\ s^{-1}$ ("∼") of the P4-derived wind speed. Additional qualifiers are used alone or in combination with the wind speed consistency indicators: if many/all relevant MRAMS wind speeds are less than the P4 value minus $3\ m\ s^{-1}$ ("<"), and if they are more than the P4 value plus $3\ m\ s^{-1}$ (">"). A "good match" for wind speeds is thus indicated by either "=," "⩾," "$\gtrsim$," or ">." It follows that a "near match" for wind speeds is indicated by either "∼" or "$\lesssim$." An "X" or "<" indicates "no match" for wind speeds.

After evaluating fits for all 3 sols, we combine these evaluations for each L_s window as follows:

1. If at least 2 out of 3 sols are a "good match," the whole L_s bin gets a "good fit" mark and a numerical score of 2.
2. If at least 1 sol is a "good match," the whole L_s bin is considered to "sometimes fit" and gets a numerical score of 1.
3. If not a single sol is a good match, it is a "no fit" for this L_s bin and is flagged by a score of 0.

The numerical scores then get summarized into an average score for the entire portion of springtime considered (normalized by the number of L_s windows that have P4 measurements for that ROI) for wind directions and speeds separately. These scores provide a numerical way to evaluate the goodness of fit over all relevant available P4 data. As with any average score, it obscures the winds' variability within the springtime. This attempt at general classification is difficult given each ROI's specifics of location, local topography, relationship to nearby large-scale features, and seasonal observational coverage. For example, the quality of fits can be different at the beginning of spring versus later in the season because atmospheric conditions shift significantly with seasonal ice coverage. However, we found such general classification useful, if not fully correct, because it allows us to examine where the atmospheric modeling more robustly reflects the P4-inferred wind direction and where it exhibits clear shortfalls.

As can be seen in Table 2, the fits of wind direction are good at most of the ROIs, while the fits for wind speeds are not as good. This is not a surprising outcome because, as we mentioned above, estimates of wind speeds from P4 are much less constrained compared to wind directions because of the multiple assumptions that had to be made. More work is needed to better understand the specifics of CO_2 jet eruptions and to narrow the parameter space of physical parameters describing them.

We have loosely categorized our ROIs into three categories according to the overall quality of their fits. This is accomplished by computing a weighted mean of the average seasonal direction match score (weight of 0.67) and the average seasonal speed score (weight of 0.33)—this value is shown in the last column of Table 2, along with one of the following fit categories:

1. Category I (⩾1.80): a good fit consistent throughout the season, with wind directions and speeds predominantly matching between P4 data and MRAMS output.
2. Category II (⩾1.30): a partial or more inconsistent fit. Some ROIs that got a "good fit" score for wind direction can still fall into this category if their wind speeds match inconsistently between either L_s bins or individual sols. Winds at ROIs in this category can match well for a part of the overall springtime season considered but match poorly for the remainder. A multitude of potential factors (anything that can alter the modeled wind velocities) may explain the less good fits. One of these is if important complexity of surrounding or local topography is not resolved by the current MRAMS configuration. The CO_2 jets also may not be active after some point in the spring (ROI dependent). Other potential model-relevant factors include uncaptured variations in surface albedo and emissivity of the surface ice cover, or even a poor match to the actual vertical loading of atmospheric dust (not well known at these high-latitude sites).
3. Category III (<1.30): a particularly inconsistent or poor fit.

Out of the 27 ROIs we investigated, there are 10 ROIs in Category I, 11 in Category II, and 2 in Category III. For four ROIs we could not make a classification owing to a lack of P4 data. Below we show and discuss an example from each of categories I and II, along with the two Category III ROIs. These descriptions also serve as an explanation on how to read/interpret the plots for the rest of the ROIs that are included in Appendix B. Following that, brief synopses of our results at each of the remaining ROIs are provided.

6.1. Category I Example: Giza

Below we describe results for ROI Giza (84.8 °S, 65.7 °E) in detail. We chose Giza for this because it has consistent P4 data coverage for every L_s interval through the study season and the fit between MRAMS model and P4 data is consistently good.

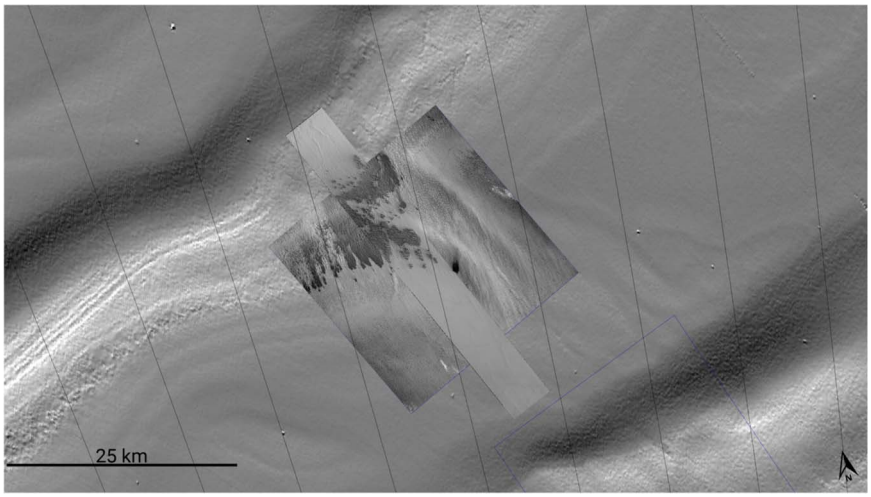

Figure 11. Context of ROI Giza (84.8 °S, 65.7 °E). The background image is MOLA shaded relief, the first insert is a CTX context image (G10_022273_0952_XN_84S294W), and the narrow highest-resolution insert is HiRISE image ESP_020150_0950_RED. Meridian lines are spaced 2° apart. Direction to north is noted in the lower right corner.

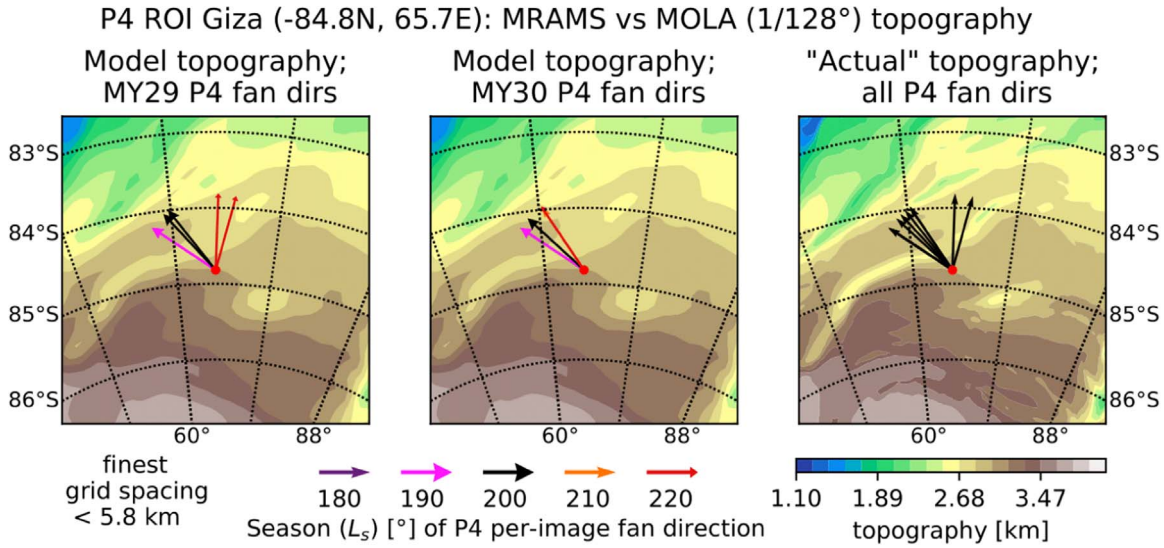

Figure 12. Topography of ROI Giza (an approximately 240 km × 240 km area). The left panel shows the topography used by the MRAMS model overlaid with arrows that represent wind directions derived from P4 data for MY29. Arrows that show P4 data are color-coded for L_s ranges. The middle panel is the same but shows P4 data for MY30. The gridded MOLA 1/128° data set (one of the highest-resolution topography data sets available) is contoured in the right panel and is overlaid by all MY29 and MY30 P4 fan directions ($L_s \approx 180°$–$220°$).

It is often insightful to understand the context of the location under discussion, as well as its topographical setting. The south polar region of Mars is topographically complex, with large craters, plateaus, scarps, and the like. Subsequently, each ROI has unique local and nearby features (along with spatially complex seasonal ice emplacement/sublimation) that modulate its environment and winds. Furthermore, the topography and surface characteristic fields used by any numerical model are constrained by both the model's finite grid spacing and the resolution/accuracy of available observational data sets—it is always important to realize how reality differs from what the model "sees." Even so, at many ROIs the MRAMS configuration used in the work captures much of the relevant topographic detail. To accompany our comparisons of modeled and inferred winds, contextual imagery and topographic context maps for all ROIs are included in Appendix B.

Figure 11 puts one of the HiRISE images measured by P4 (narrowest image in the figure) at ROI Giza into a broader context with a wider CTX image underneath, and MOLA (grayscale) shaded relief in the background. The dark lobes that are evident in the images are fields of myriad dark fan-shaped deposits atop the seasonal CO_2 ice. In these snapshots they are chiefly situated on a modest equator-facing slope. Giza is located near a small outcrop of SPLD, and the local surface is relatively smooth with only a few small craters visible. Figure 12 contains a comparison of the MRAMS topography used for this work (left and middle panels) with the higher-resolution MOLA 1/128° topographic data set (right panel) for ROI Giza—the area shown is a few times larger than that shown in Figure 11. The two topographic fields are generally similar at this ROI, with the narrower valleys/ridges being smoothed out in the model field—note that there is more than a kilometer of vertical relief in the area shown. However, the overall orientations of the valleys, ridges, and plateaus are resolved by MRAMS.

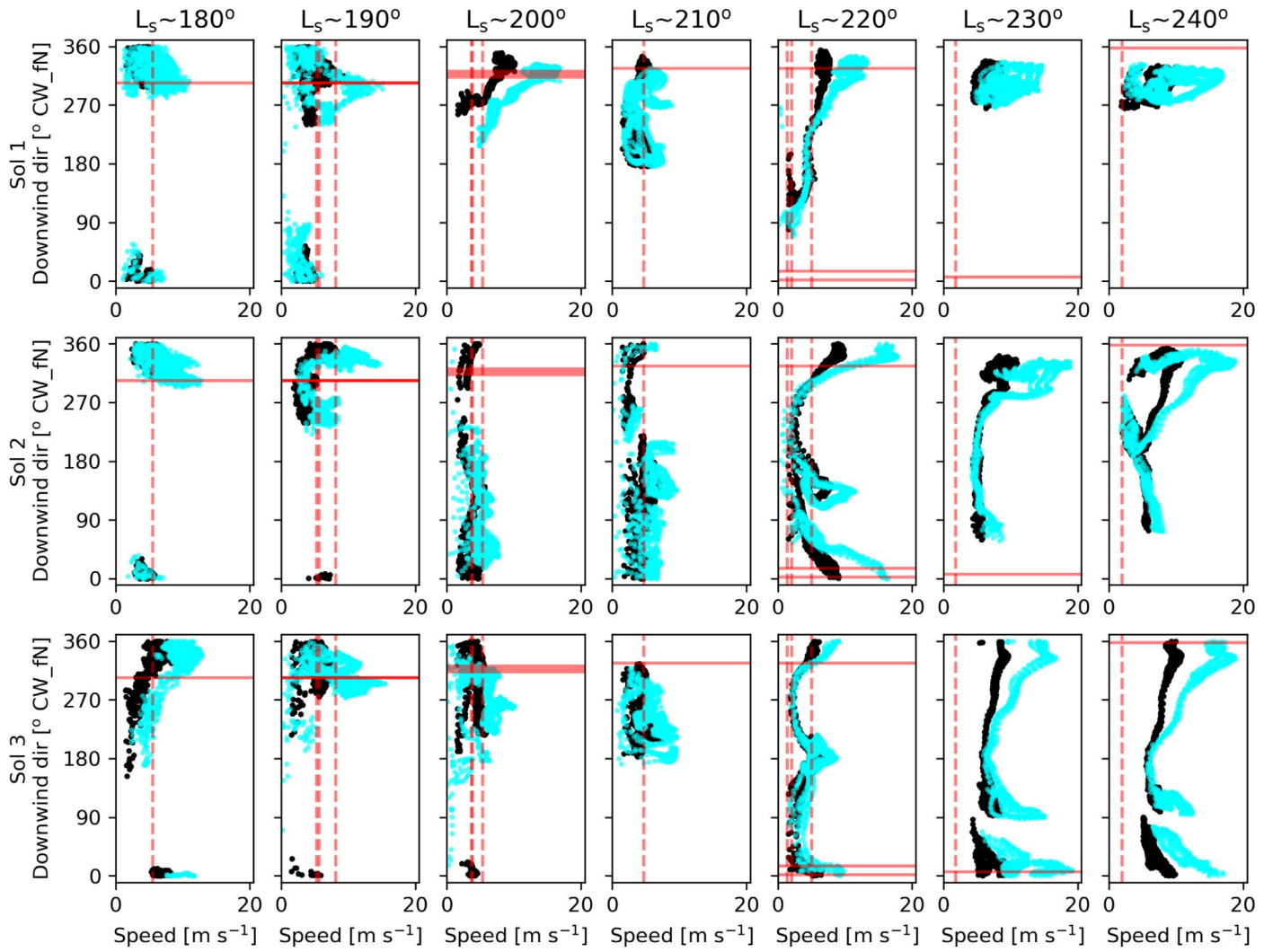

Figure 13. P4–MRAMS comparison at Giza for 3 consecutive sols in the MRAMS run. Each column is a 10° step in L_s, and each row represents 1 sol (as described in Section 5.1). Panels show scatter plots of downwind directions and speeds from MRAMS, with values from ∼5 m AGL shown in black and those from ∼91 m shown in cyan, indicating the level of wind velocity variance within the lowest 100 m of the atmosphere. All horizontal grid points within 8.3 km of the ROI centroid are shown. Solid horizontal red lines indicate fan directions derived from P4 results, and dashed vertical red lines indicate wind speeds estimated from P4 results. Several lines in one L_s bin indicate that multiple HiRISE images acquired during this L_s period were measured by P4. Note that the wind variability within each sol is due to changes in local and regional solar heating throughout each day, interacting with topography and regional-scale circulations. The level of variability between sols in each L_s window is most likely due to transient regional-scale atmospheric eddies (vs. some sort of model spin-up effect).

A relatively simple conceptual model of near-surface winds in the south polar region of Mars during early spring chiefly includes cold/dense katabatic flows heading locally downhill and a more diffuse sublimation flow oriented toward the equator—both of these are subject to the Coriolis effect, which nudges a northward (equatorward) flow to the left in the direction of movement (i.e., toward the northwest and west). Later in the season, the seasonal ice becomes increasingly patchy and more stochastic local and regional thermal and baroclinic circulations become superposed on the former pattern—more day-to-day (and intraday) wind variability would be expected in this period.

Figure 12 also shows the P4-derived wind directions at ROI Giza for MY 29 and MY 30, color-coded by L_s window. Note that although the orientation vectors are displayed as if they were 60 km long (for easy viewing), they are most likely only valid at a much smaller scale (near the circle at the vectors' origin). The P4-inferred flow toward the NW is consistent with downhill katabatic/sublimation flow acted upon by the Coriolis effect. The multiple inferred wind directions at $L_s \approx 220°$ (although in two different years) are probably due to more stochastic baroclinic circulations in midspring.

Figure 13 shows an example of P4-to-MRAMS comparison for ROI Giza, with columns representing seasonal progression from left ($L_s \approx 180°$) to right ($L_s \approx 240°$). Rows are the 3 consecutive sols from the MRAMS output (as described in Section 5.1). Vertical dashed lines on the plots show P4-derived wind speeds, and horizontal lines indicate P4-measured fan directions (assumed to be the downwind direction). Dashed lines were chosen intentionally for wind speed to signal that those values must be considered more cautiously owing to multiple assumptions associated with the P4 wind speed estimates. The plotted points represent MRAMS-predicted winds at two different altitudes AGL. Those that are black are from ∼5 m AGL, while those in cyan are from ∼91 m AGL. This type of figure is designed to illustrate the variability of winds within the lowest 100 m of the atmosphere (i.e., encompassing the maximum height assumed for the CO_2 jets)

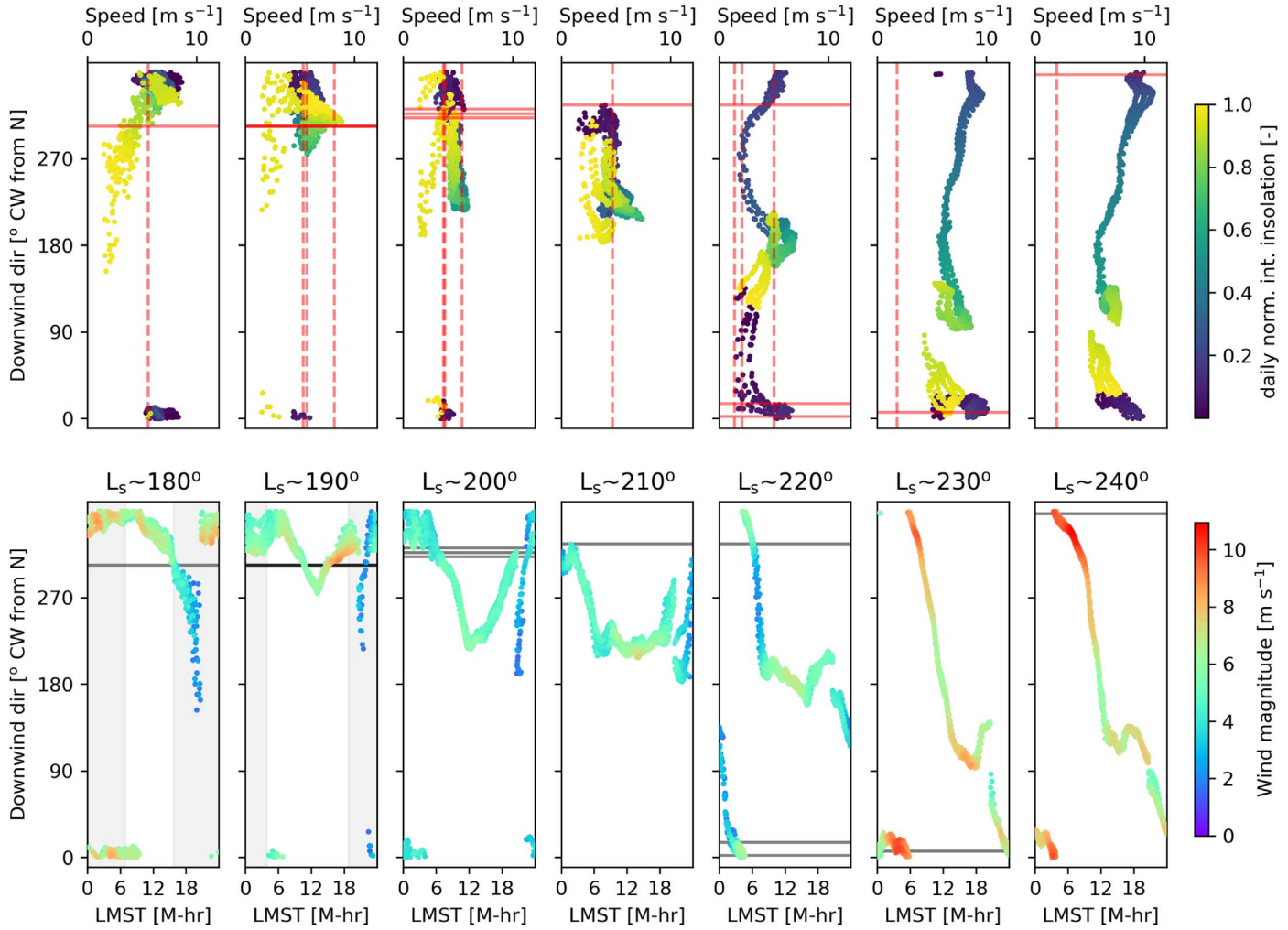

Figure 14. P4–MRAMS comparison at Giza. Each column is a 10° step in L_s and shows sol 3 model output. All horizontal grid points within 8.3 km of the ROI centroid are shown. Top: scatter plots of downwind directions and speeds from MRAMS ~5 m AGL colored by the daily integrated insolation. Solid horizontal red lines indicate fan directions derived from P4 results, and dashed vertical red lines indicate wind speeds estimated from P4 results. Bottom: scatter plots of downwind direction from MRAMS vs. LMST in Mars hours, colored by wind magnitude. Black lines are P4 wind directions. Shaded regions indicate local night at this location.

at this ROI. Note that the wind variability within each sol is due to changes in local and regional solar heating throughout each day, interacting with topography and regional-scale circulations. The level of variability between sols in each L_s window is most likely due to transient regional-scale atmospheric eddies (vs. some sort of model spin-up effect).

The presence of several vertical and horizontal red lines on the same subplot indicates that several HiRISE images were acquired during the L_s interval between this subplot and the previous one. If any of those lines are instead gray (none at this ROI), it indicates that multiple disparate fan directions are present within each HiRISE image. In the case of Giza (Figure 13), there was just one HiRISE image acquired between $L_s \approx 175°$ and $L_s \approx 185°$, three images between $L_s \approx 185°$ and $L_s \approx 195°$, and so on.

At Giza, P4 data fit well to MRAMS model output for both derived wind speeds and fan directions between $L_s \approx 180°$ and $L_s \approx 210°$. There are some differences between sols, with some being more stable (sols 1 and 3), while sol 2 exhibits modeled wind directions that shift through virtually all directions starting at $L_s \approx 200°$. Nevertheless, in all 3 sols during this early spring period, P4-derived speeds and directions have corresponding MRAMS values within the tolerances described at the beginning of Section 7. Note that it is common at this ROI for the MRAMS winds to be strongest at or near the P4-inferred wind direction(s).

That is not to say that partial ambiguities do not exist at this ROI. For example, between $L_s \approx 200°$ and $L_s \approx 210°$ the directions and lengths of P4 fans do not change much. However, MRAMS winds during these L_s windows vary in direction during the day significantly more than at earlier L_s, and there are many fewer values that match the P4 directions satisfactorily. This could indicate that there are no (or few) new CO_2 jet deposits being created during the $L_s \approx 210°$ window, and thus the fan orientations do not reflect the more variable wind directions estimated by MRAMS during that same period. Alternatively, the CO_2 jets (and thus fans) may require certain special conditions to occur—perhaps particular times of day and/or strong winds—strongly limiting the range of modeled wind directions that are relevant.

Later, at $L_s \approx 220°$, some P4-measured fan orientations show a clear shift from northwest to north or north–northeast, but the fans are not particularly long (e.g., at $L_s \approx 190°$ the fans are significantly longer). MRAMS also shows a change in behavior with winds now varying widely through the day for all 3 sols, but the P4-inferred wind directions occur when the winds (and

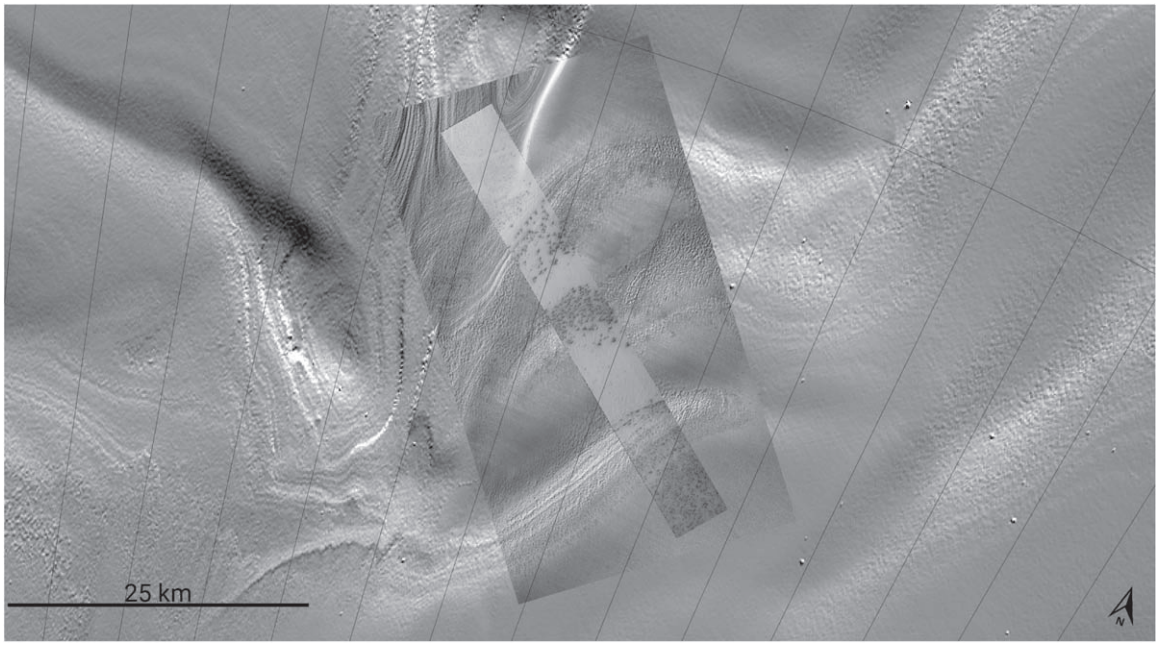

Figure 15. Context of ROI Manhattan Classic (86.4 °S, 99 °E). The background image is MOLA shaded relief, the first insert is a CTX context image (G12_022971_0936_XN_86S261W), and the narrowest highest-resolution insert is HiRISE image ESP_011394_0935_RED. Meridian lines are spaced 2° apart. Direction to north is noted in the lower right corner.

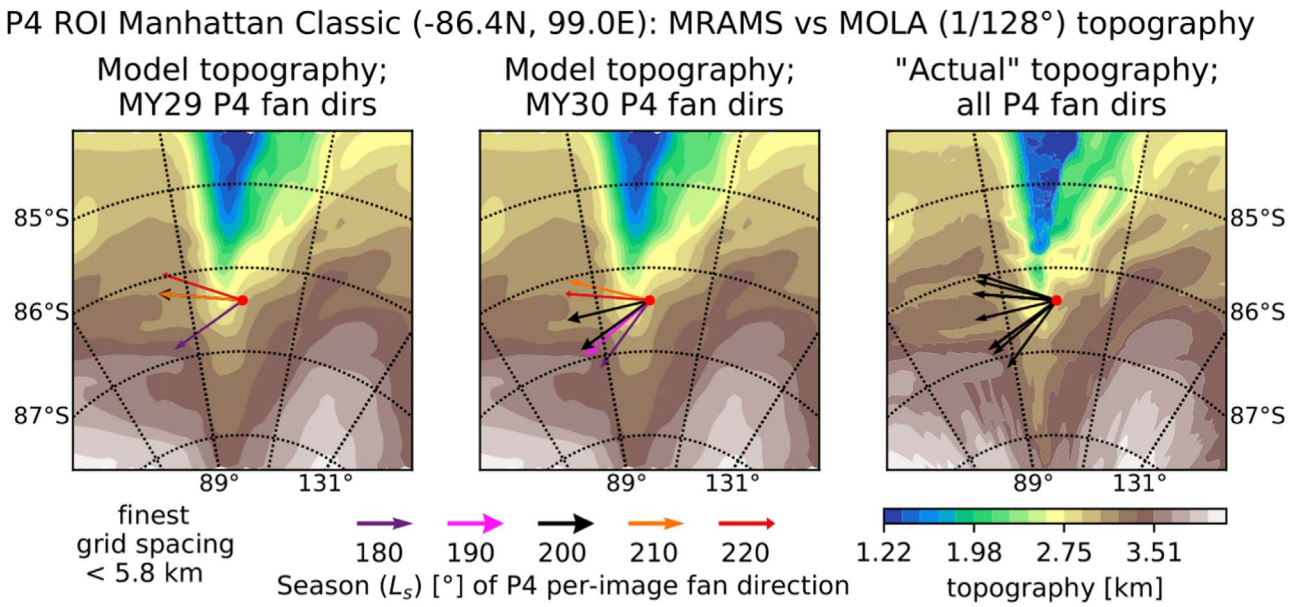

Figure 16. Topography of ROI Manhattan Classic, overlaid by early spring P4-measured fan directions. Data visualization is as in Figure 12 (an approximately 240 km × 240 km area). This ROI is located on the east side of a deep valley (the head of Chasma Australe, with at least 1.3 km elevation change). The MRAMS topographic resolution is able to capture most features well, with the exception of the narrow secondary and tertiary SPLD troughs.

vertical wind shear) are strongest. This fan direction shift could thus potentially be due to redistribution of the material already on the ground by strong winds, and not active jet eruptions—perhaps consistent with the above suggestion of jet activity ceasing at this ROI before the $L_s \approx 210^\circ$ window.

At $L_s \approx 230^\circ$ and $L_s \approx 240^\circ$ P4 and MRAMS wind directions match in only 3 out of the 6 sols of MRAMS output analyzed, again when winds are strong. The P4-measured fan lengths are also quite short, which is poorly consistent with CO_2 jet activity occurring during periods of strong winds. Also, note that P4-inferred winds are less robust for this time interval and ROI owing to patches of relatively thin (and thus lower-albedo) surface CO_2 ice. Overall, our results are more consistent with no CO_2 jet activity at Giza during these L_s windows.

Figure 14 presents a different view of the same MRAMS and P4 data for Giza during sol 3 of each L_s window. The first row of plots in the figure is similar to the bottom row of Figure 13, except that only winds from the lowest model are shown and the points are colored by their daily normalized integrated insolation (DNII) values. This DNII quantity is zero at local midnight and is a measure of the time-integrated insolation energy that has reached the ice surface by each model output time step (normalized to a maximum value of unity). It is intended to approximately highlight times of day when solar

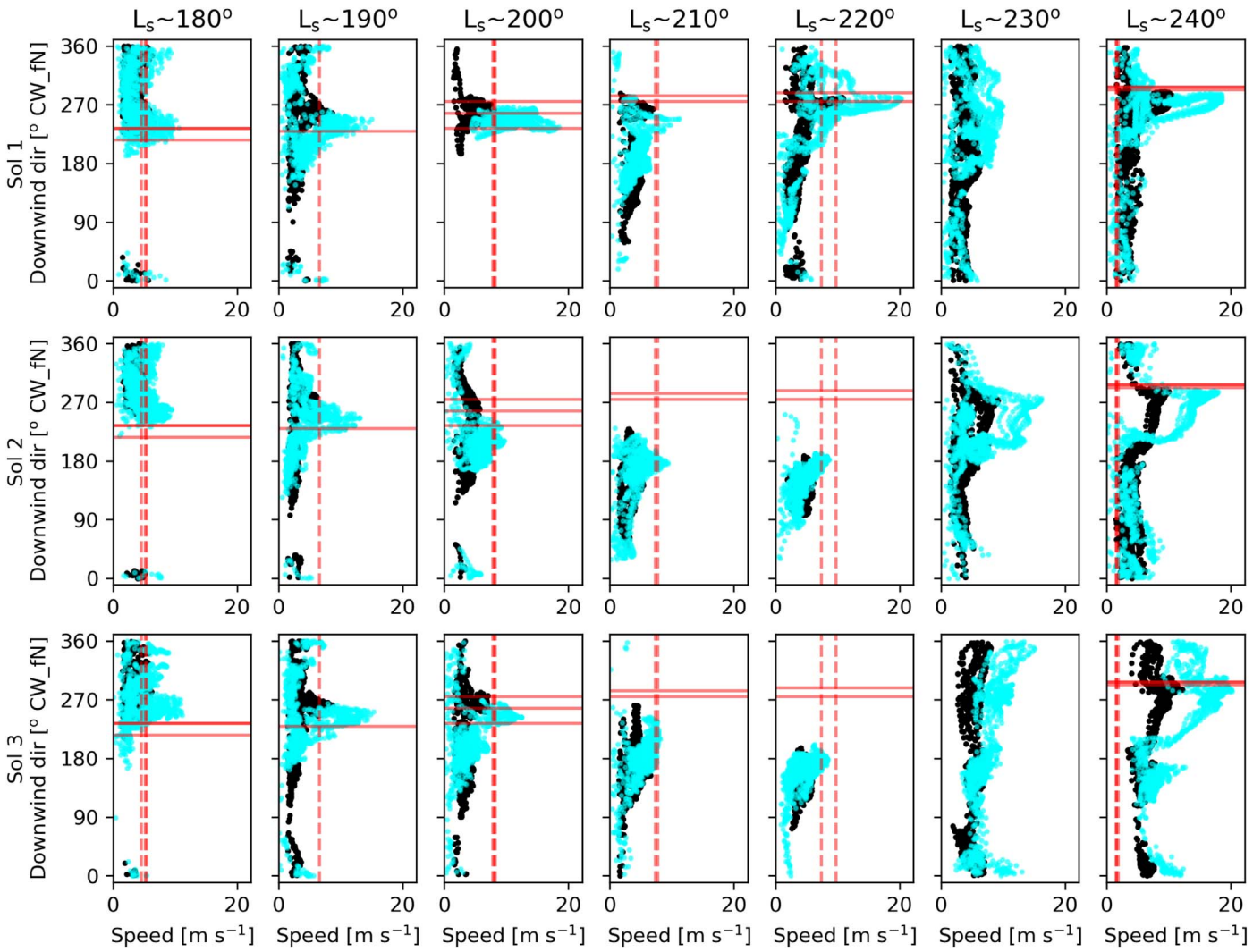

Figure 17. P4–MRAMS comparison at Manhattan Classic. Data visualization is as in Figure 13. Here, the fit between P4-derived and MRAMS wind directions is quite good for sol 1, while fits for sols 2 and 3 are inconsistent. There is a tendency for the wind direction matches to be when the modeled winds are strongest. The 91 m/5 m vertical wind shear is minimal (or even negative) until later in spring.

energy may be actively sublimating CO_2 gas on the underside of the slab ice, as hypothesized by the Kieffer model. Note that DNII is zero until the Sun rises, has a value of 0.5 near local noon, and reaches a value of 1 at sunset (and remains 1 until midnight, crudely representing the potential ability of energy stored in the subsurface earlier in the day to affect the jet process). For $L_s \approx 180°$ through $L_s \approx 200°$ at ROI Giza, MRAMS wind directions match P4-inferred values when DNII is generally >0.5. However, for the later L_s windows the DNII is generally very small when the P4 and MRAMS wind directions match. One possible way of interpreting this is that CO_2 jets are active in the afternoon and/or early evening during the $L_s \approx 180°$ through $L_s \approx 200°$ windows but cease to be active after that.

The second row of plots in Figure 14 still shows downwind direction on the *y*-axis, but the *x*-axis is now local Mars solar time (LMST) in Mars hours. Points representing MRAMS-simulated downwind directions are colored according to the simulated wind speeds, and black horizontal lines represent P4 fan directions. Shaded areas indicate the times when the Sun is below the horizon (nighttime) for this ROI. At Giza, the Sun does not set at and after about $L_s \approx 200°$—when the season progresses into so-called "polar day." The Sun during the polar day goes up and down (low in the sky) with respect to the horizon but never sets below it, while constantly changing its azimuth. This creates special illumination conditions where nearly all inclined surfaces collect solar energy more efficiently than flat ground. In this setting, the local topography might be a defining factor with regard to the level of CO_2 jet activity. This series of plots is intended to more clearly indicate the time(s) of day when MRAMS and P4 wind directions match (and therefore when the jet eruptions may occur). Even so, at ROI Giza no consistent jet eruption time of day is evident.

6.2. Category II Example: Manhattan Classic

Note that there are three ROIs with names that start with "Manhattan" that lie within 1° of latitude from each other: Manhattan Classic (86.4 °S, 99 °E), Manhattan Cracks (86.2 °S, 99 °E), and Manhattan Frontinella (87 °S, 99.1 °E). They all share a similar topographic setting and are Category II sites, but Manhattan Classic has P4 fan measurements for more L_s windows than the other two.

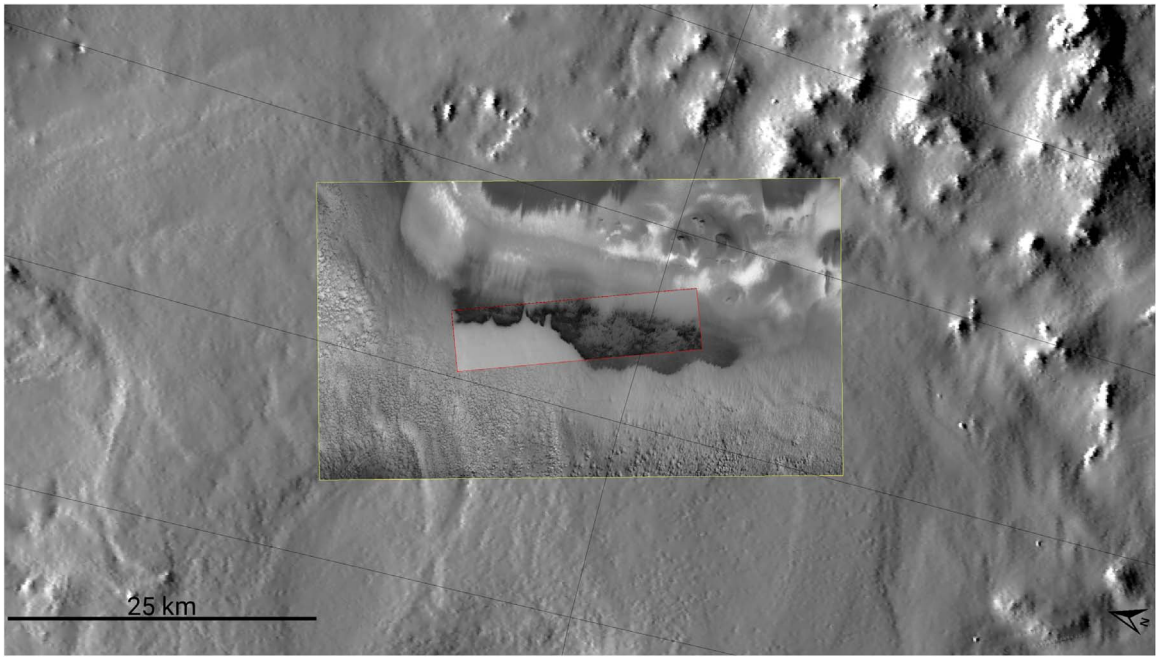

Figure 18. Context of ROI Buenos Aires (81.9 °S, 4.8 °E). The background image is MOLA shaded relief, the first insert is a CTX context image (B12_014284_0980_XN_82S355W), and the narrow highest-resolution insert is HiRISE image ESP_011792_0980_RED. Meridian lines are spaced 2° apart. Direction to north is noted in the lower right corner.

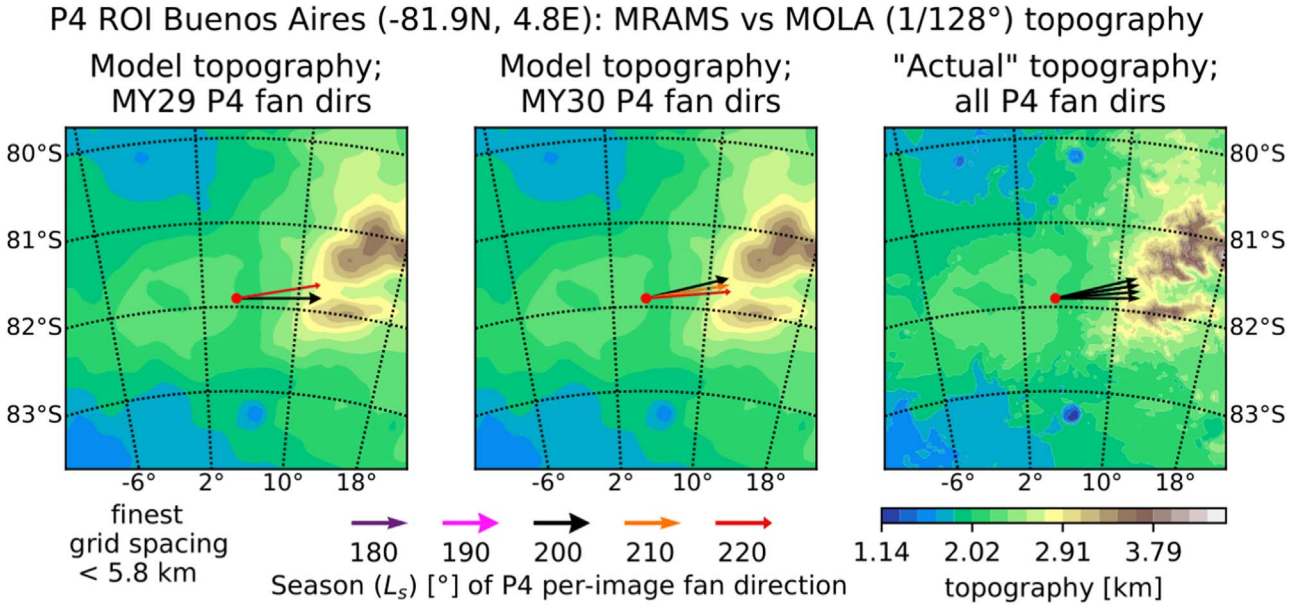

Figure 19. Topography of ROI Buenos Aires, overlaid by early spring P4-measured fan directions. Data visualization is as in Figure 12 (an approximately 240 km × 240 km area). This ROI is located west of an isolated mountain range (with peaks about 1.5 km above the dark fans). The MRAMS topographic resolution is able to capture most medium-scale features well, but not the narrow hills and mountain peaks.

From the context information in Figure 15 we can see that ROI Manhattan Classic is situated on complex terrain and includes several differently oriented slopes. Looking at the topography alone, in Figure 16 we see that Manhattan Classic is situated near the head of Chasma Australe. Furthermore, all of the Manhattan ROIs are located on the eastern side of the chasma (see Appendix B), with the topography near Manhattan Classic being the most complex. One might be tempted to assume that cold springtime near-surface airflow so close to such a large valley would be oriented parallel to and down the valley—and the model output indicates that wind deeper within Chasma Australe does just that. However, the air flowing down the chasma has to originate from somewhere, and MRAMS indicates that it flows approximately westward off the SPLD lobe to the east, crosses the Manhattan ROIs, and descends into the chasma. Later in the spring season, differential sublimation of seasonal ices (and heating of patchy ice-free areas) on the various local slopes may also modulate the wind—this is much

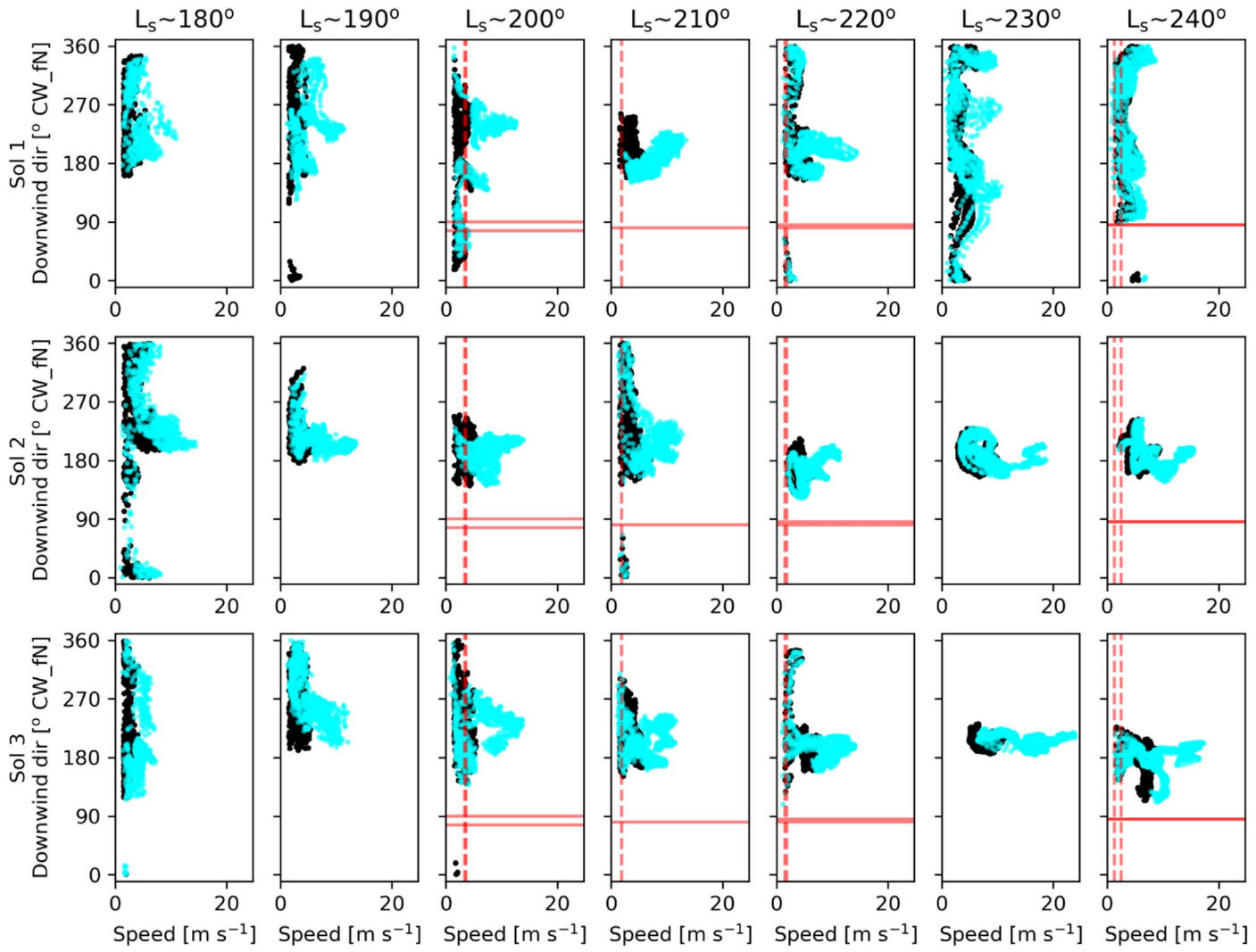

Figure 20. P4–MRAMS comparison at Buenos Aires. Data visualization is as in Figure 13. The MRAMS and P4-inferred wind directions only rarely match well at this ROI.

more challenging for atmospheric modeling to capture. The P4-measured fan directions in Figure 16 are consistent with the schematic flows described above, with fans oriented SW and W–SW during the earliest L_s windows and toward the W–NW later.

Figure 17 shows a P4–MRAMS comparison for ROI Manhattan Classic. Similar plots for Manhattan Cracks and Manhattan Frontinella can be found in Appendix B. At the earliest observed $L_s \approx 180°$, the fit between MRAMS and P4 5 m and 91 m AGL wind directions and speeds for Manhattan Classic is inconsistent for sol 2—only the modeled 91 m AGL winds on sol 2 exhibit a near match to the P4-inferred values. Later during the $L_s \approx 200°$ window, Manhattan Classic modeled winds generally match with the P4 data for wind directions, but the associated speeds poorly fit for two-thirds of the sols (the 91 m wind speeds get closest to matching). At $L_s \approx 210°$ and $L_s \approx 220°$ wind directions do not match between the model and P4 in 2 out of 3 sols (even at the 91 m level). During this period, P4 data indicate significantly higher derived wind speeds than the MRAMS model predicts at ~5 m AGL (but the wind speeds higher above the ground match). At $L_s \approx 240°$ the situation changes to a good fit for wind directions and a somewhat poor fit for speeds, with P4-inferred wind speeds being on the smaller side of simulated speeds.

Similar to at ROI Giza, there is a clear tendency at Manhattan Classic for the wind direction matches to be when the modeled winds are strongest. The 91m-to-5 m vertical wind shear (Figure 17) is often minimal (and even solidly negative) at this ROI, indicating shallow flows of relatively dense air that hug the surface (e.g., katabatic winds). At this ROI there does not appear to be a clear time of day that the CO_2 jet eruptions prefer to occur at (see Appendix B).

6.3. Category III—Buenos Aires and Schenectady

In this category there are two ROIs—Buenos Aires and Schenectady. These illustrate two different cases of unusually severe mismatch between MRAMS and P4-derived wind directions and speeds. To determine why, we delve into the rich details that our dual approach (spacecraft imagery + mesoscale atmospheric modeling) provides.

ROI Buenos Aires (81.9 °S, 4.8 °E) is a roughly 25 km long north–south-oriented patch of dark fans situated just west of some hilly and mountainous terrain (Figure 18). Looking at the topography (Figure 19), these fans are located on the western

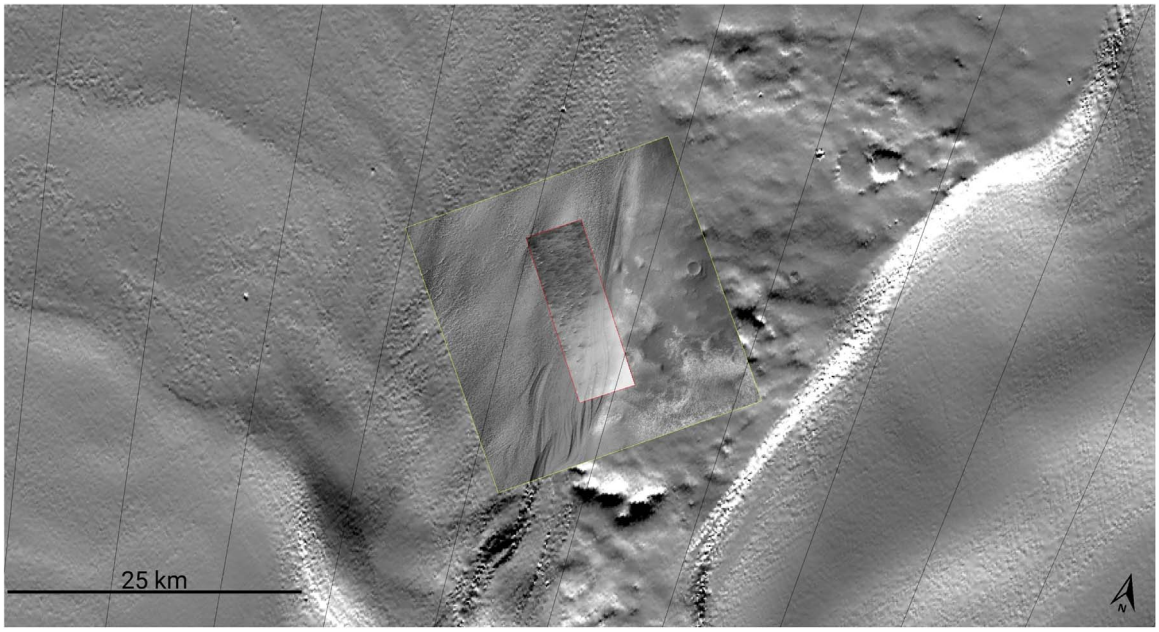

Figure 21. Context of ROI Schenectady (85.0 °S, 95.0 °E). The background image is MOLA shaded relief, the first insert is a CTX context image (G10_022114_0950_XN_85S265W), and the narrowest highest-resolution insert is HiRISE image ESP_011921_0950_RED. Meridian lines are spaced 2° apart. Direction to north is noted in the lower right corner.

edge of a modest valley, and the hilly terrain seen to the east in Figure 18 is on a slope leading upward to the edge of an isolated mountain range approximately 40 km to the east. It is difficult to predict a priori what the diurnal near-surface airflow might be at this ROI, as, unlike Giza and Manhattan Classic, it is relatively far from the SPLD (and their substantial modulation of airflow). However, katabatic flow toward the west (originating in the mountains to the east) might be expected at "night" (the portion of the polar day when the insolation is weakest)—if no other regional flows eclipse them.

Table 2 indicates that at ROI Buenos Aires there are no P4 measurements for the $L_s \approx 180°$, 190°, and 230° seasonal windows. The modeled and P4-inferred wind directions do not match at all for the 210° and 220° L_s bins and only match for 1 out of 3 sols within the other two L_s windows.

Figure 20 (top row) shows sol 3 of the P4-to-MRAMS comparison for ROI Buenos Aires. It (and the full plot containing all 3 sols in Appendix B) shows that the dominant near-surface airflow in the MRAMS output is toward the south or southwest (roughly parallel to the eastern mountains). This flow appears to be due to a complex combination of regional circulations to the north and south. Meanwhile, the available P4 fan directions are toward the east or E–NE (upslope toward the eastern mountains).

In HiRISE imagery from $L_s \approx 182°$–195° (not measured by P4) at Buenos Aires there appear to be multiple fan orientations at each vent that are more consistent with the MRAMS wind directions at those L_s. The HiRISE data then indicate that starting around $L_s \approx 196°$ the eastward fan orientations become more common, and they are dominant by $L_s \approx 206°$—especially in the north and central parts of the ROI. Furthermore, MRAMS output from only 10 km to the east (81.9 °S, 6.0 °E); Figure 20, bottom row) shows wind directions that match the P4-inferred ones—this is only two model grid points away from the ROI centroid. The 3D model output (not shown) also indicates that as the insolation gets stronger in early spring at this ROI, differential heating of the air over the mountains to the east during midday induces upslope flow. Thus, it appears that the apparent severe mismatch between MRAMS and P4-inferred wind directions at ROI Buenos Aires is probably merely due to insufficient horizontal spatial resolution in the model that does not resolve the full complexity of the hilly slope and mountains to the east. The lack of P4 measurements for the earlier L_s windows also played a role in its current categorization.

ROI Schenectady (85.0 °S, 95.0 °E) is located on the western slope of Chasma Australe, down valley of the Manhattan ROIs. Only one HiRISE image of this area was analyzed by P4 (shown in Figure 21). Even so, for that image we have robust fan statistics with smooth distributions for both derived wind speeds and inferred directions. Figure 21 shows the context of ROI Schenectady, with the dark fans in the HiRISE image (acquired at $L_s \approx 207°.3$) located midslope, but avoiding the valley floor. The associated model topography (Figure 22) indicates that the horizontal resolution of the model configuration used here broadens the lateral slopes of Chasma Australe and poorly resolves the secondary and tertiary SPLD troughs. It also shows that the P4-inferred fan direction during the $L_s \approx 210°$ window is toward the northeast—consistent with katabatic flow into the chasma.

Table 2 indicates that at ROI Schenectady there was a match between P4-inferred and MRAMS wind directions on sol 1, but only near matches during the other 2 sols. Modeled wind speeds were also consistently much lower than the P4-derived value, cementing the Category III classification for this ROI. Figure 23 (top row) shows sol 2 of the P4-to-MRAMS comparison for ROI Schenectady. It (and the full plot containing all 3 sols in Appendix B) shows that modeled wind directions at/near the P4-measured fan direction are more common during five out of the seven L_s bins. Having P4 measurements at other seasonal windows would have likely helped this ROI remain in Category II. Furthermore, MRAMS

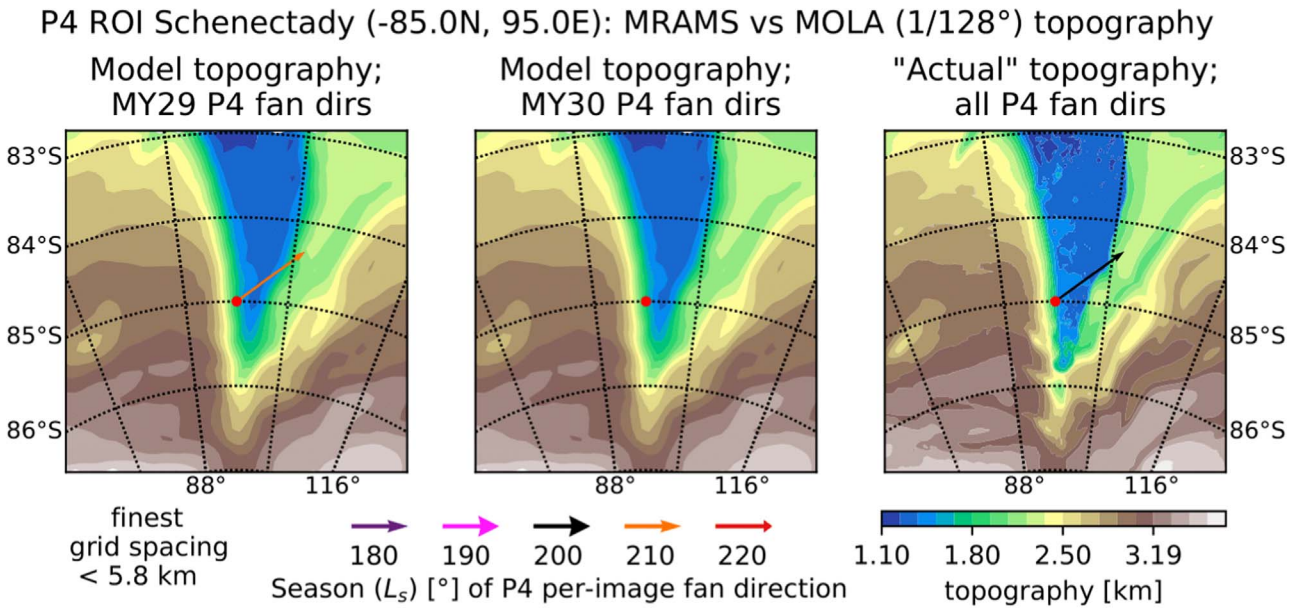

Figure 22. Topography of ROI Schenectady, overlaid by early spring P4-measured fan directions. Data visualization is as in Figure 12 (an approximately 240 km × 240 km area). This ROI is located on the western slope of Chasma Australe, down valley of the Manhattan ROIs. The MRAMS topographic resolution is able to capture most features well, with the notable exception of the narrow secondary and tertiary SPLD troughs. The model topography also broadens the lateral slopes of the chasma.

output from only 12 km to the west (85.0 °S, 92.6 °E; Figure 20, bottom row) shows wind directions that match the P4-inferred ones—this is only two model grid points away from the ROI centroid. Thus, it appears that the apparent mismatch between MRAMS and P4-inferred wind directions at ROI Schenectady is probably merely due to insufficient horizontal spatial resolution in the model that unrealistically broadens the lateral slope of Chasma Australe, leading to relevant wind direction shifts occurring farther west than is accurate.

6.4. Remaining ROIs

In the text below we list specific notes for the rest of the ROIs listed in Table 2. We include several of the most relevant associated plots to aid discussions of wind behavior at some ROIs. All other plots (P4–MRAMS comparisons, topographic maps, and context images) for these ROIs can be found in Appendix B.

Albany (81.93°S, 60.4 °E), Category I: Topographically, Albany is located on a relatively smooth equator-facing slope at the edge of the SLPD. P4 measured fans at this ROI starting at $L_s \approx 221°$, and the resulting wind speed and direction estimates fit well to the analogous fields from MRAMS. According to MRAMS, at earlier seasons ($L_s \approx 180°$–$220°$) the wind direction with the strongest winds (and strongest wind shear) remains quite stable, even matching well with the later-season P4-inferred wind directions. The direction of these winds is consistent with katabatic flows descending from the SPLD. Thus, MRAMS does not provide any obvious additional information about when the fans that were observed at ROI Albany by HiRISE were created.

Atka (86.98°S, 169.7 °E), Category II: Topographic variations near this ROI are extreme: depressions, high hills, valleys, and the ragged edge of the SPLD exhibit, representing over 1 km of relief. Note that there is a deep north-to-south depression just southeast of Atka that the current MRAMS grid configuration does not resolve. It is not clear from the context alone what the primary wind direction(s) might be. For this high-latitude ROI, there are three P4-analyzed HiRISE images: the first was acquired at $L_s \approx 212°$, the second at $L_s \approx 243°$, and the third at $L_s \approx 250°$. The fit between MRAMS and P4 is better for the first image ($L_s \approx 210°$ window) and barely satisfactory for the second ($L_s \approx 240°$ window), with 2 out of 3 sols not matching well. Similar to Albany, the modeled wind pattern is relatively stable prior to $L_s \approx 210°$ and shows a dominant wind direction that is near the measured fan direction at $L_s \approx 210°$. Note that both the P4–MRAMS wind direction match and near match at $L_s \approx 240°$ did not coincide with strong winds. The last image did not provide good P4 fan statistics, which indicates that by $L_s \approx 250°$ the fan deposits visually blended in with the underlying substrate.

Bilbao (87 °S, 127.3 °E), Category II: This ROI is located at relatively high altitude on a lobe of the SPLD, with the topographic gradient downhill in all cardinal directions except south. Note that there are significant SPLD troughs that MRAMS resolves poorly. In this setting one might expect Bilbao to experience katabatic flow directed toward the north and west. The P4-inferred wind directions shift from toward the west at $L_s \approx 180°$ to toward the northwest by $L_s \approx 200°$ and then appear to rotate further clockwise (to N–NE) by $L_s \approx 230°$. The fit between P4-inferred and MRAMS wind directions is overall good (but inconsistent between sols) at $L_s \approx 180°$–$190°$, but it worsens in the $L_s \approx 200°$ window. MRAMS wind speeds near the matching wind directions are generally not consistent with the P4-derived ones throughout this early part of the season—instead, the direction of the strongest winds seen in the MRAMS results is about 180° from the P4-inferred ones. This indicates that the model prefers directing flow down the opposite side of the SPLD lobe, but perhaps this preference would be reversed if the model had better resolved the nearby SPLD troughs. Later at $L_s \approx 230°$–$240°$, there are MRAMS wind directions (coincident with strong winds and wind shear) that match P4 results, but

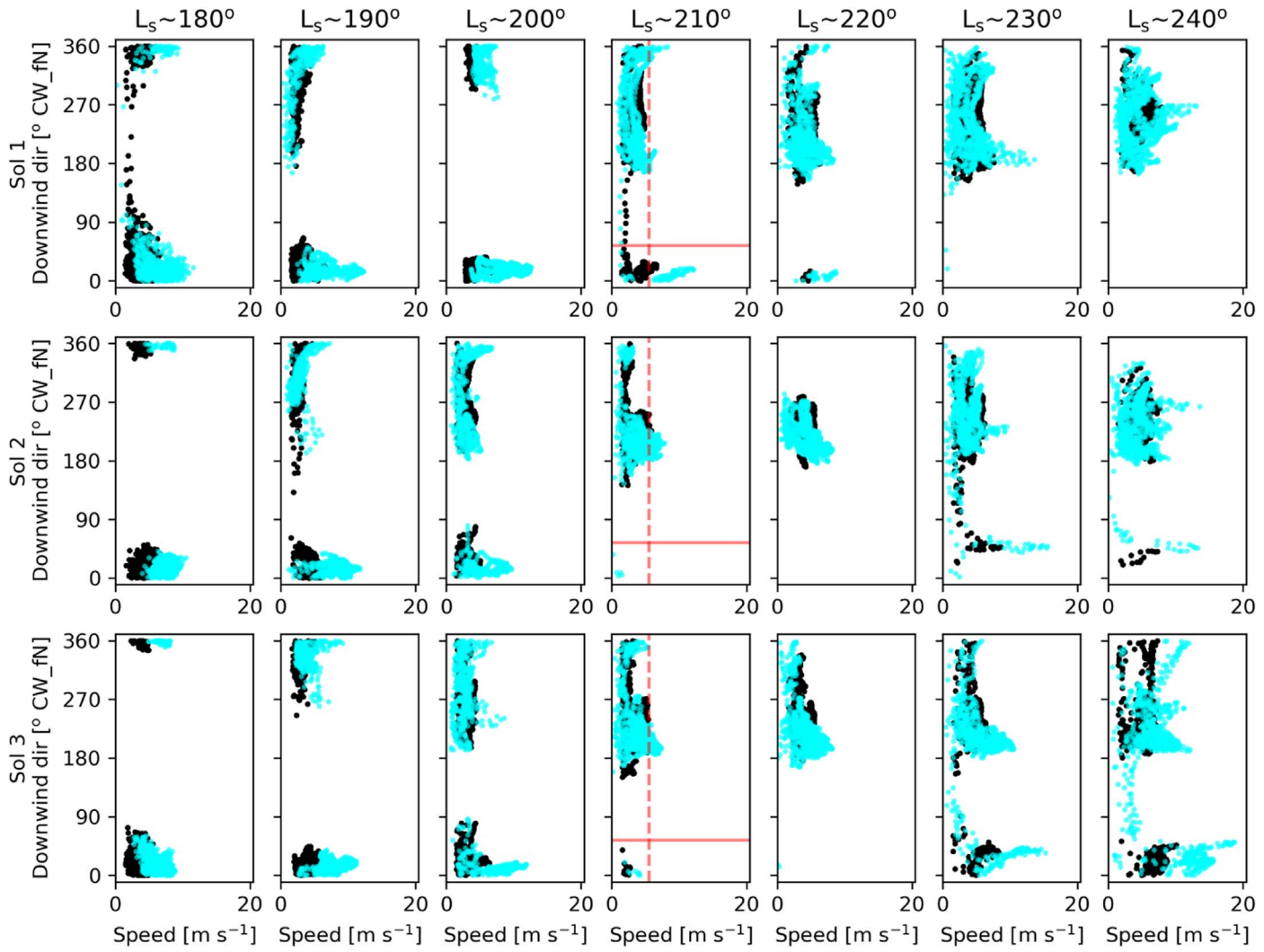

Figure 23. P4–MRAMS comparison at Schenectady. Data visualization is as in Figure 13. The MRAMS and P4-inferred wind directions only match during 1 sol at this ROI (and even then, only for several model snapshots).

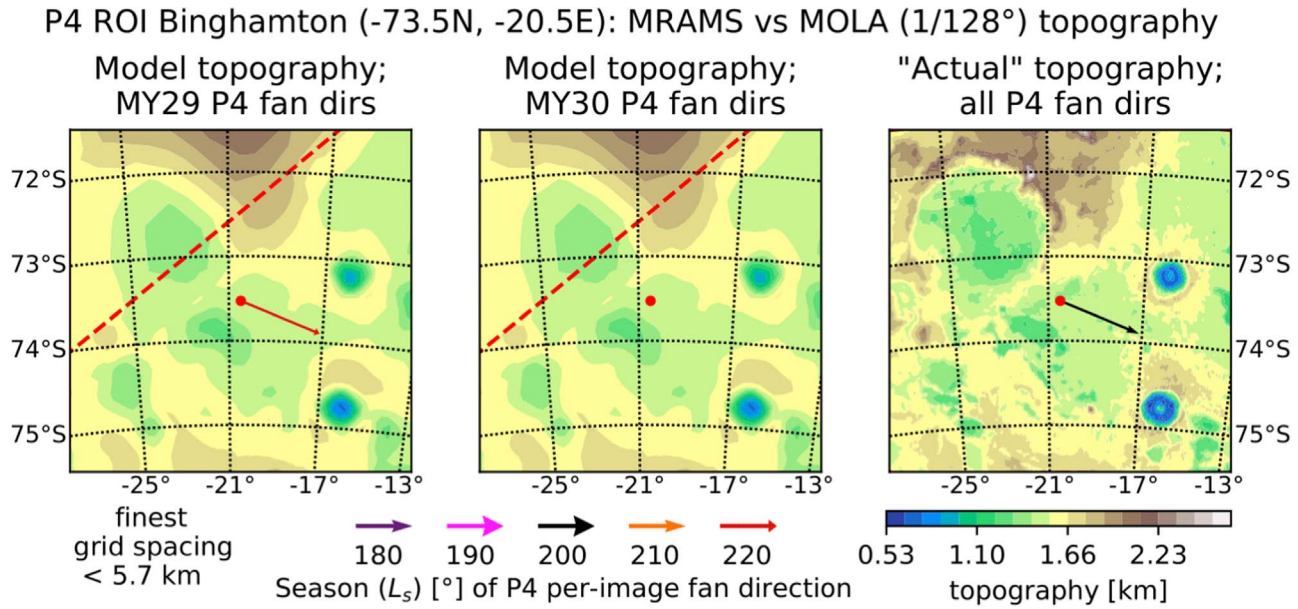

Figure 24. Topography of ROI Binghamton (an approximately 240 km × 240 km area), overlaid by early spring P4-measured fan directions. Data visualization is as in Figure 12. Binghamton was only observed in MY29, and only one HiRISE image yielded fan statistics robust enough to estimate wind properties. The dashed red line indicates where the edge of MRAMS grid #4 is.

they occur near local midnight when insolation is at a minimum (note that the Sun never sets at ROI Bilbao at these L_s). This is unexpected because the Kieffer model of jet/fan occurrence is driven by insolation. However, perhaps residual pent-up gas pressure under the ice slab (produced at times of day with greater insolation) is only able to be released when the ice is more brittle.

Binghamton (73.53°S, 339.5 °E), Category I: This is our most equatorward ROI and is located in the heavily cratered southern highlands, in a basin near higher terrain in the north (Figure 24). Binghamton has a P4-analyzed HiRISE image at $L_s \approx 223°$ that indicates a wind direction (E–SE) and speed that is a good match to the MRAMS results in the $L_s \approx 220°$ window. The MRAMS results indicate that from $L_s \approx 180°$ to 210° the primary wind direction is between east and southeast, consistent with the later P4 results. However, during the $L_s \approx 220°$ window as the seasonal cap edge draws nearer, a second flow regime is established (blowing toward the west and southwest), and it becomes more dominant as the season wears on. Late in the spring, at $L_s \approx 254°$, P4 data show that there are no longer any visible fans.

Buffalo (82.5°S, 80 °E), no category: This ROI is located near the edge of the SPLD, where, again, the current MRAMS resolution cannot resolve the troughs well. Despite having two HIRISE images for this ROI—at $L_s \approx 224°$ and 241°—the P4 fan statistics are poor here and prohibit us from estimating any wind properties. There are two possible explanations for the citizen scientists not marking many fans at those L_s: either CO_2 jet activity in this location is infrequent then, or the wind is calm at the time of jet eruptions (leading to spots/blotches, not fans). The MRAMS results indicate that the strongest early spring winds at Buffalo generally flow toward the northwest and west, but by the $L_s \approx 210°$ window, the strongest winds flow more toward the southwest. MRAMS indicates that the near-surface wind direction with the strongest wind speeds becomes much more variable at and after the $L_s \approx 220°$ window but does not indicate a slowdown of the winds as the poor P4 statistics might suggest—instead, the winds significantly increase in magnitude. This suggests that the jets at ROI Buffalo may be largely inactive by $L_s \approx 224°$.

Caterpillar (74.22°S, 168.5 °E), Category I: This is the second most equatorward ROI and is situated on a plateau within complex terrain, north of a regional ridge. The current MRAMS configuration resolves many of the salient topographic features, but many nearby smaller craters and valleys are poorly resolved. P4 analyzed one HiRISE image at $L_s \approx 196°$, and those data show a main wind direction peak, as well as a little secondary peak. MRAMS simulations also show a two-peaked distribution of wind directions on some sols in the early spring. Despite the complex topographic setting, MRAMS results match the P4-inferred wind directions well during the $L_s \approx 200°$ window—once again, MRAMS wind speeds (and vertical wind shear) are strongest at the matching wind directions.

Cortland (82.69°S, 273.1 °E), no category: Situated within the jagged northern edge of an SPLD lobe, much of the important topography near this ROI is not resolved well by the current MRAMS configuration. P4 fan statistics are too poor here to calculate the dominant wind direction. MRAMS results indicate moderately strong winds at Cortland, with two main wind directions in early spring—one toward the northwest and west one, and another toward the northeast and east.

Geneseo (85.18°S, 92 °E), no category: This ROI is located high upon the western slope of Chasma Australe, southwest of ROI Schenectady. It lies near an SPLD trough that is not well resolved by the current MRAMS configuration. P4 fan statistics are too poor here to calculate the dominant wind direction. In early spring, MRAMS indicates moderate winds toward the northeast, north, and northwest at Geneseo. Later in the spring, the wind directions become more variable, but the strongest modeled winds blow toward the E–NE.

Halifax (87°S, 72.3 °E), Category I: This ROI is on a broad slope at the eastern edge of an SPLD lobe, with some SPLD troughs relatively nearby. The head of Chasma Australe is about 100 km downhill toward the northeast, and it might be expected that katabatic flows would generally follow this path. P4-inferred winds are available at $L_s \approx 214°$ and match well with MRAMS output in the $L_s \approx 210°$ window, although this match occurs near local midnight. Note that the modeled 91 m/5 m wind shear peaks near the matching wind direction.

Inca City (81.38°S, 295.8 °E), Category II: This is probably the most challenging location among our ROIs for both P4 analysis and atmospheric modeling because of its local topography that includes 300 m high ridges arranged in square patterns (that the current MRAMS configuration cannot resolve). More generally, Inca City is located on the northeast side of a sizable ridge, with higher-elevation regional topography to the west and south. The near-surface winds here would appear to be affected by both the influences of mesoscale atmospheric dynamics and very localized insolation-driven phenomena related to the slopes of the local ridges mentioned above. Thus, it is surprising to see a good fit between P4-inferred and MRAMS wind directions (Figure 25) in the early spring. P4 fan directions predominantly point downhill on the sides of the local ridges. Even so, the first fans (i.e., within the $L_s \approx 180°$ window) appear on the equator-facing slopes of those ridges because these slopes are the first to be illuminated by the early spring Sun. Later fans appear on the other slopes, resulting in a secondary peak that appears in the P4 fan direction histograms. One can follow the development of the second peak (as well as the third, fourth, up to the seventh peak) in the wind direction histograms in Figure 26. It may or may not be a coincidence that the two dominant P4-inferred wind directions generally coincide with the two dominant flow directions in the MRAMS results (toward the NW/W–NW and E–NE/NE). In the context of the larger-scale topography, winds toward the northwest would be flowing roughly parallel to and around the sizable ridge that Inca City is located upon, and winds toward the northeast would be flowing downhill perpendicular to the slope (like katabatic flow). The deflection of (and drag on) the cold airflow by the local steep ridges at this ROI may either modulate this larger-scale flow or mimic it. During the $L_s \approx 230°$ and 240° windows, the MRAMS wind directions only inconsistently match the P4-inferred ones—perhaps the unresolved effects of the local ridges are more important at these times.

Ithaca (85.13°S, 180.7 °E), Category II: Located just north of a weakness in the SPLD, this ROI has a broad regional plateau to its north and channels, depressions, and mesas to the south. One might expect katabatic flows to generally be directed southward here and be turned toward the left (east in this case) by the Coriolis effect. Indeed, in the early spring P4-inferred wind directions are generally toward the E–SE at Ithaca, matching the MRAMS results well through the

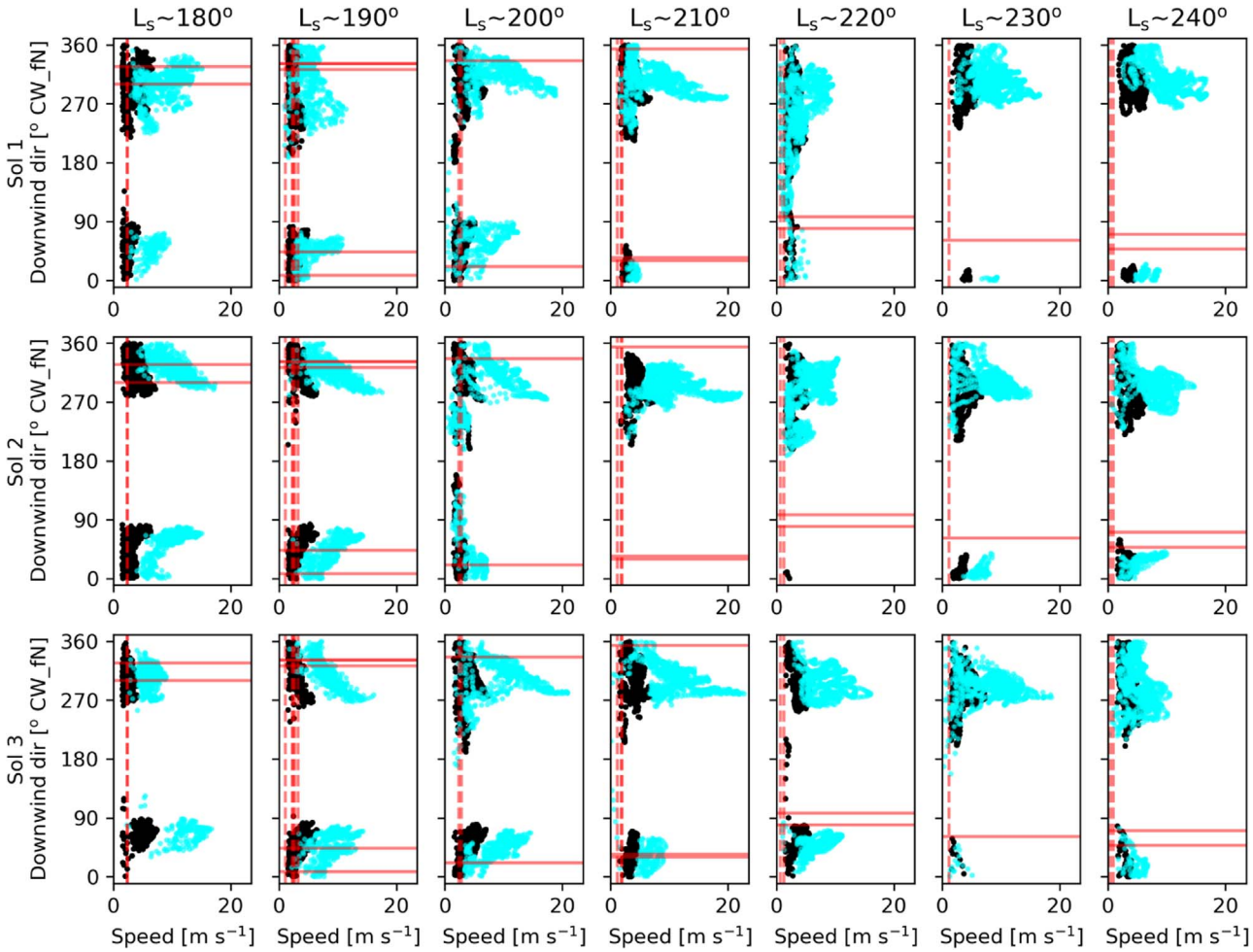

Figure 25. P4–MRAMS comparison at Inca City. Data visualization is as in Figure 13. A bimodal wind direction regime is evident during early spring in both the MRAMS and P4 results.

$L_s \approx 200°$ window. During the $L_s \approx 210°$ window, MRAMS wind directions have shifted further toward the east and nearly match the P4 results. The strongest winds and vertical wind shear occur at/near the matching wind directions during the early spring period. MRAMS results indicate that the wind directions become more variable during the $L_s \approx 230°$ and 240° windows, and where the wind directions match between P4 and MRAMS in the $L_s \approx 240°$ bin, wind speeds are not consistently strong. At ROI Ithaca the P4-inferred wind direction does not strongly change throughout the spring. This is an unusual case among our ROIs and means that from P4 data alone we cannot determine whether the fans seen in the second image of the seasonal sequence are new fans or they are the same ones that appeared already in the first image of that sequence.

Macclesfield (85.4°S, 103.9 °E), Category II: This ROI is located on a relatively narrow ridge of the SPLD east of and overlooking Chasma Australe. This ridge is resolved partially, but not well, by the current MRAMS configuration. As with the other ROIs near Chasma Australe, one might expect overall flow to be directed toward the chasma. At Macclesfield, P4 fan distributions show a peculiar feature—one wind direction dominates the distribution in the early spring, but after $L_s \approx 190°$ a secondary peak appears. It indicates flow in almost the opposite direction of the primary peak, and at $L_s \approx 214°$ it has almost as many fans as the dominant direction (see the histogram in Figure 6). MRAMS results only show hints of a strongly bimodal wind direction distribution at this location, but they do strongly reproduce the main P4-inferred direction. Overall, the MRAMS and P4-inferred wind directions match well, except for MRAMS not exhibiting the secondary peak during the $L_s \approx 200°$ window. The dominant P4-inferred wind direction keeps shifting slowly until the end of the spring interval studied here, which suggests that new fan deposits are being created even later in spring. We propose an explanation for this behavior: Macclesfield has two distinct areas, one of which (the western portion of the ROI) has a slope more favorable for early CO_2 activity. CO_2 jets start erupting in this area and are directed by the winds dominant at early L_s. Later in spring, the other area (the eastern portion of the ROI) becomes active. By this time not only have the atmospheric dynamics shifted and the dominant winds changed, but the time of jet eruptions might have shifted as well. We do not know how big this shift is, but it is reasonable to expect a shift, especially at the beginning of the polar day season. At the latitude of Macclesfield polar day begins at around $L_s \approx 200°$, coinciding with the first appearance of the secondary peak in P4-inferred wind directions.

Oswego Edge (87°S, 86.4 °E), Category II: This ROI is perched above and just southwest of the head of Chasma Australe, and again one might generally expect katabatic flows into and down the chasma. A large SPLD trough lies just to the north, but it is not well resolved by the current MRAMS

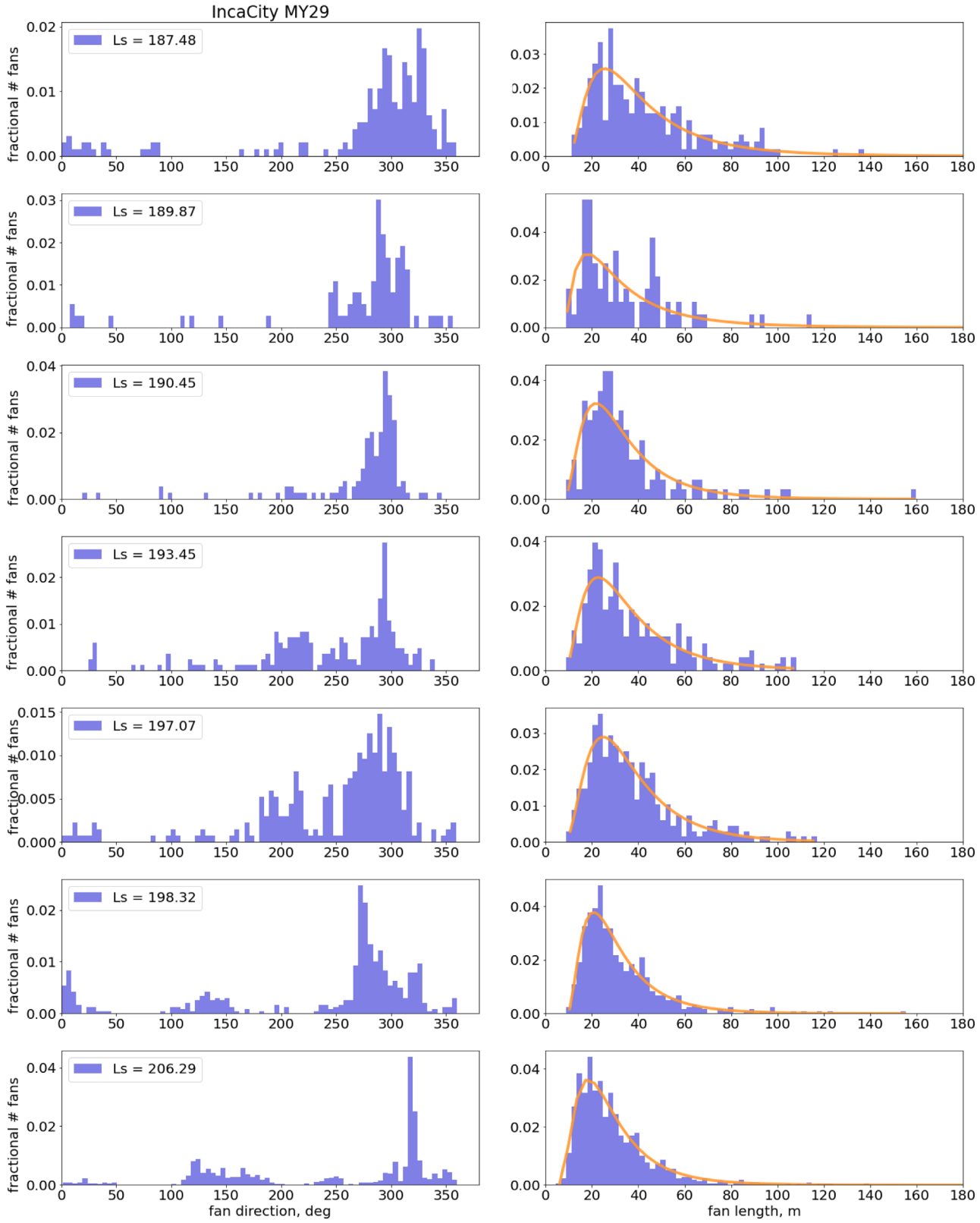

Figure 26. Fan direction (left) and length (right) distributions at ROI Inca City. Data visualization is similar to Figure 5, with the difference that we avoided plotting curve fits to the fan direction histograms. Fan directions show multiple peaks in their distribution. Their directions roughly coincide with downslope directions on the sides of local topographic ridges at this ROI.

configuration. P4 wind directions consistently match well with MRAMS model results, but early in the spring the associated MRAMS wind speeds are often too weak to match the P4-derived ones well. However, later in the season (during and after the $L_s \approx 230^\circ$ window) the P4-derived and MRAMS wind speeds (near the matching wind direction) are consistent with

each other. The less-than-ideal resolution of the MRAMS topography may be driving the early spring wind speed inconsistencies.

Pisaq (86.8°S, 178.0 °E), Category I: This ROI is situated within a deep depression/channel, surrounded by irregular pieces of SPLD highlands. Despite the complex topography, the current MRAMS configuration captures most nearby important topographic features well. At Pisaq, P4 data exhibit a bimodal distribution for wind directions that is only weakly pronounced at $L_s \approx 215°$ but becomes stronger by $L_s \approx 235°$. Some of the fans that point to different directions have a common source, proving that the bimodal distribution here is due to the wind changing with time between different jet eruptions and not because of spatial variability of the wind. The P4-inferred wind directions are consistent with katabatic flow from the higher terrain immediately to its southwest. MRAMS results do not show a similar bimodal distribution during the $L_s \approx 210°$ window. However, by the $L_s \approx 220°$ bin the model has a similar bimodal wind direction distribution for the strongest winds. Overall, the MRAMS and P4 winds match well at Pisaq, but the fit is less robust near $L_s \approx 210°$.

Portsmouth (87.3°S, 167.8 °E), Category I: Located about 40 km southwest of Pisaq, this ROI is located in a higher-elevation depression/channel at the foot of the SPLD lobe that crosses the south pole. The current MRAMS configuration cannot resolve many of the nearby smaller troughs and ridges. Portsmouth has P4-inferred wind directions that are nearly constant from about $L_s \approx 200°$ to 240°. MRAMS simulations show that while the modeled wind directions vary widely throughout the day, the wind speeds at most directions are weak. In early spring (before about $L_s \approx 205°$), the stronger MRAMS winds are generally oriented toward the east (within $\pm 30°$ or so). For the rest of the spring season, the strongest modeled winds generally blow northward (within $\pm 30°$). These stronger winds are consistent with katabatic flow off the SPLD lobe to the south and occur at local times when the insolation is low. MRAMS winds match those derived from P4 measurements well at this ROI.

Potsdam (81.68°S, 66.3 °E), Category I: This ROI is located on a broad equator-facing slope at the edge of the SPLD. The nearby topography is generally well resolved by the current MRAMS configuration. Here one might expect katabatic flows from the higher reaches of the SPLD to be directed downslope and turned left (further toward the west) by the Coriolis effect. The P4-inferred wind directions are consistent with this—directed toward the west early in the season, and gradually becoming toward the northwest later in the season—and match well with the strongest MRAMS winds.

Rochester (83.2°S, 158.4 °E), no category: Situated on a high part of the SPLD between two deep chasmas (Figure 27), the topography near this ROI is generally well represented in the current MRAMS configuration. P4 analyzed three HiRISE images acquired from $L_s \approx 220°$–240°. All of these images have too few fans for reasonable statistics, but they curiously have a large number of small dark blotches. This is an unusual situation among our ROIs, as it superficially implies nearly calm winds during the jet eruptions. However, the MRAMS results indicate the presence of moderate to strong winds at Rochester throughout the spring season considered, at many times of day. There may be a few explanations for this: (1) The location is somehow protected by local topography, and there is effectively no wind that could deflect 100 m tall CO_2 jets to create fan-shaped deposits. This seems unlikely based on the available imagery and topography data. (2) The blotches observed by P4 may be the result of very short (in height) CO_2 jets that do not "feel" the winds much. (3) The blotches might be sublimation spots on the ground, and not formed by CO_2 jets at all. We prefer the second hypothesis. All three HiRISE images for this ROI were acquired relatively late in spring, when the seasonal CO_2 layer is thinning, and when we would expect jet eruptions to become weak or stop entirely. Even so, the surface albedo signature of a weak eruption and direct surface sublimation would be effectively indistinguishable from each other.

Starburst (81.8°S, 76.1 °E), Category I: Located on a broad equator-facing slope at the edge of the SPLD, this ROI lies to the east of Potsdam. The nearby topography is generally well resolved by the current MRAMS configuration but misses some of the nearby SPLD troughs. The winds here would be expected to be similar to that at Potsdam. The P4 data for Starburst have good fan statistics until $L_s \approx 213°$, after which the number of blotches significantly overtakes the number of fans, suggesting that the CO_2 jets may be much weaker later in midspring. MRAMS fits P4 wind directions well, generally when modeled wind speeds are greatest (even when blotches are common in midspring). This suggests a situation similar to ROI Rochester, where the CO_2 jets are weak and thus short in height.

Taichung (82.3°S, 306 °E), Category II: This ROI is located immediately to the north of a ragged SPLD edge. There is complex smaller-scale topography nearby, particularly toward the west, that MRAMS does not resolve well with its current configuration. P4 analyzed a single HiRISE image acquired at $L_s \approx 228°$ that shows a bimodal wind direction distribution with the two peaks at 320° and 41° (clockwise from north; toward the northwest and northeast, respectively). The main fan direction (toward the northwest) coincides well with the dominant winds in the MRAMS results, and the model indicates that that flow persists through the spring season studied. The secondary wind direction (toward the northeast) inferred by P4 at $L_s \approx 228°$ is robustly present in the MRAMS results at and before the $L_s \approx 220°$ window. This may indicate that the northeast-oriented fan deposits at Taichung were created before $L_s \approx 228°$.

Troy (85.02°S, 259 °E), Category I: This ROI is situated within a broad (but rough) valley/channel near the edge of the SPLD. The current MRAMS configuration does not resolve the small-scale complex topography nearby. The earliest HiRISE image in Troy was acquired at $L_s \approx 181°$ and has 195 blotches and just four fans. Thus, we are unable to draw any direct conclusions about the wind distributions at this early L_s using P4. This is similar to the situation at ROI Rochester, with the difference that at Troy the image with almost no fans was taken quite early in spring. It is unreasonable to assume that the jet activity has stopped by that L_s or that sublimation could expose patches of the surface substrate. If there were no fans and no blotches, we could assume that CO_2 jet activity has not started yet, but the presence of a significant number of blotches contradicts this. Thus, two possibilities remain: that this ROI generally does not have strong winds at the beginning of spring at the time of day that the jets are erupting, or that CO_2 jets at and just before this L_s are very weak and therefore short in height. The MRAMS results show a variety of wind speeds at Troy during the $L_s \approx 180°$ window, with stronger winds

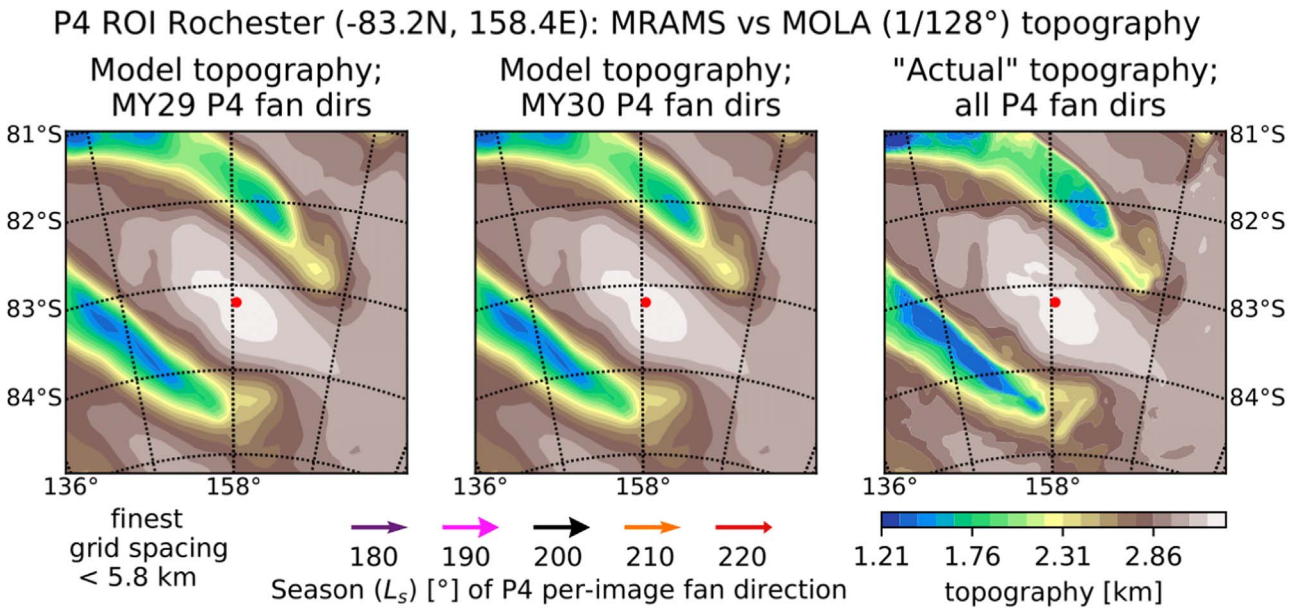

Figure 27. Topography of ROI Rochester (an approximately 240 km × 240 km area). Data visualization is as in Figure 12. This ROI is situated on a high part of the SPLD between two deep chasmas. No robust P4-measured fan directions were made here during the L_s range shown.

blowing toward the E–NE and W–SW (both consistent with flow through the valley that it is located within) and much weaker winds at other directions. The next HiRISE image here was acquired at $L_s \approx 244°$. It shows a bimodal distribution of fan directions with peaks at 99° and 147° (clockwise from north; toward the east and southeast, respectively). MRAMS fits these directions well in 2 out of 3 sols during the $L_s \approx 240°$ window, although the strongest winds predicted by MRAMS at that L_s are toward the west.

Wellington (82.2°S, 225.2 °E), Category II: Located on the slope of a smaller SPLD trough, winds at this ROI might be expected to be oriented generally toward the northeast (i.e., downhill). However, the current configuration of MRAMS does not resolve the associated SPLD trough well. Two HiRISE images at Wellington were analyzed by P4: the first at $L_s \approx 178°$ and the second at $L_s \approx 211°$. The first image exhibits a distribution of fan directions with one maximum (at 99°; toward the east), while the second one shows a bimodal distribution with the two dominant wind directions at 36° and 76° (toward the northeast and E–NE, respectively). MRAMS modeling indicates a low wind direction variance at this ROI in early spring, increasing greatly in midspring. Note that the MRAMS wind directions during the $L_s \approx 200°$ window would match the P4-measured fan directions at $L_s \approx 211°$ very well, so perhaps the CO_2 jets had already ceased to be active by the time that image was acquired.

7. Conclusions

The analysis of HiRISE images by the P4 project resulted in the determination of fan deposit orientations (assumed to be the wind directions at the time of the CO_2 jet eruptions) and lengths (from which we inferred wind magnitudes using particle sedimentation calculations) at 27 ROIs around the southern polar region during the spring season. The seasonal markings change considerably from one HiRISE image to another at most of these ROIs, and thus intraseasonal variations in wind speeds and directions can be derived. HiRISE, and consequently P4, data provide us with a new way to investigate seasonal processes on Mars with potential for quantitative analysis.

We used the MRAMS to estimate the wind speeds and directions within the lowest 100 m of the atmosphere for the entire south circumpolar region poleward of 70 °S, with a mesoscale horizontal grid spacing of <5.8 km at all of the studied ROIs during consecutive springtime 10° L_s windows. At the beginning of spring ($L_s \approx 180°$) in that icy circumpolar region, the dominant airflows are easily influenced by topography. By $L_s \approx 240°$ the seasonal CO_2 ice cap has retreated drastically, and the airflow across this region is consequently much more dynamic, with transient cap-edge and baroclinic circulations strongly modulating the flows over the remaining (rapidly sublimating) seasonal ice cap. Modeled instantaneous wind speeds and directions do vary over the approximately 100 m height of an erupting jet, but the vast majority of those variations are consistent with the metrics of the observed fans.

For the first time, model-derived and imagery-derived wind directions and speeds have been compared for 27 ROIs. Overall, MRAMS wind directions (and, to a lesser extent, wind magnitudes) are consistent with those measured by P4 at 25 ROIs. Even so, at most ROIs the match between winds from MRAMS and P4 is not consistently satisfactory for every individual 10° L_s window between the beginning and end of the spring season—the matches are often better in the early spring, but at some ROIs they are better later in the season. The fact that P4-inferred and model-estimated wind directions best match at early L_s supports the theory that the fans are created by wind blowing the material entrained in the jet as it is erupting and not just via ballistic trajectories from an angled vent. If fans were created by jets erupting through angled vents (and affected by winds minimally), then their directions would be more random with respect to the modeled winds. P4 data are also the most reliable in early spring when surface processes have not yet influenced the appearances of the fans. Later in the spring, as more patches of bare ground can be confused with deposits and jet activity has slowed or stopped with the thinning CO_2 ice, a poorer match between the P4

measurements and MRAMS is not surprising. Thus, the enhanced correlation between P4 fan direction data and model winds in early spring is a clear sign of strong interaction between the lowest reaches of the atmosphere and mineral material entrained by the active CO_2 jets.

Looking at the wind speeds alone, there are some trends between the magnitudes of MRAMS-estimated and P4-derived values. At some, mostly earlier, L_s the modeled speeds are less than than P4-derived ones, but the majority of MRAMS wind speeds (at the fan direction) are greater in magnitude than their P4-derived counterparts. This is not a surprising outcome considering that P4 estimates for wind speeds are much less constrained compared to the P4-inferred wind directions because of the multiple assumptions that had to be made to calculate speeds from fan lengths. Furthermore, there is an overall tendency at many ROIs for the MRAMS and P4 wind directions to match when the MRAMS winds (and/or vertical wind shear) are at their strongest within each sol. More work to understand CO_2 jet eruptions and their strengths, timing, and ability to propel dust/regolith particles into the Martian atmosphere needs to be done before we can narrow down the parameter space of the applied calculation and determine more realistic wind speeds at the time of eruption. On the other hand, the MRAMS configuration used here (with a grid spacing of just over 5 km) also has room for improvement, especially with respect to resolving smaller-scale topography. Gridded MOLA topography is available at a maximum resolution of ~400 m, and even higher-resolution HRSC, CTX, and HiRISE digital elevation maps are available in certain locations. However, higher resolution results in greatly increased computational expense to run the model, so some compromise is necessary. Longer MRAMS simulations (i.e., more sols of output to analyze per L_s window) may also help better understand the day-to-day wind variability/statistics at each ROI.

Mars mesoscale atmospheric models have significantly improved in recent years, providing compelling estimates for the near-surface atmospheric state (including winds) at the kilometer scale. However, we currently lack in situ (or even orbital) direct measurements of near-surface winds for most of Mars, including all of the south polar region. Such data are needed to validate that the model's behavior is representative of the real Martian atmosphere. Until we are able to acquire such measurements, the next best way to observe and understand seasonal and year-to-year changes in the south polar region springtime is to use a combination of remote sensing and analysis on the scales similar to the P4 project, along with estimating what cannot be directly seen with numerical models. We have shown in this paper that the P4 project is an outstanding example of how repeated imaging of the surface can be transformed into uniquely important data on atmospheric movements and variability.

7.1. Future Work

Hansen et al. (2019) have shown that there are indications that seasonal polar activity varies between the years with and without extended (regional or global) dust storms. However, the extent of this study and the data used were limited. Since this work has shown that MRAMS can successfully fit wind directions derived from P4, questions about the influence of global dust storms on the seasonal processes in the polar regions can be studied in more detail and utilize data from more locations around the south pole. For this work, MRAMS was run with a standard dust scenario (MY24; i.e., including no large dust storms), and the P4 data used were also for the low-dust years MY29 and MY30. However, it is possible to use P4-derived winds from more dusty years and compare them to MRAMS runs using relevant atmospheric dust loading scenarios that include a regional or global dust storm.

CO_2 jet eruptions have not been directly observed so far. One of the goals of the P4–MRAMS comparison project is to try to estimate the timing of CO_2 jet eruptions to help plan remote sensing observations of these jets in action. We have not yet reached the goal of determining the time(s) of day that jet eruptions occur because of the rich detail about the winds (especially their time variability) that the mesoscale climate modeling has provided for the many ROIs considered. However, since MRAMS was successful at predicting winds consistent with P4-analyzed fans for most ROIs, this goal is not out of reach. At many ROIs the MRAMS wind direction that corresponds to the P4-derived wind occurs during a time when the Sun is well above the horizon. However, in some cases the modeled wind direction occurs in the early local evening, or even near midnight. A more detailed evaluation of this timing is outside the scope of the current paper, but we have high expectations that for ROIs with good fits (Category I) further analysis will bring additional insights into the timing of the jets.

Appendix A
Supplementary P4 Data Table

This paper is accompanied by a supplementary data file that lists P4-derived wind directions and speeds for each of the analyzed ROIs. Table 3 provides a brief description of data in each of 10 columns in that data file.

Table 3
P4-derived Wind Directions and Speeds for Each of the Supplementary Data File

Column Number	Label	Explanation
1	ROI	Informal ROI identifier
2	obsid	HiRISE image ID
3	L_s	When the image was acquired, in degrees
4	MY	Mars year when the image was acquired
5	Scale	Map scale of the HiRISE image, in m $pixel^{-1}$
6	n_fans	Total number of P4 fan markings in the HiRISE image
7	Direction	Most probable fan direction over the whole HiRISE image calculated using a Weibull or double-Gaussian curve fit to the fan direction histogram. Units are degrees clockwise (CW) from north. If a given HiRISE image exhibits a bimodal fan direction distribution, then it will appear in two rows, with all the rest of the information repeated but with a different fan direction value.
8	FWHM	FWHM of the fan direction histogram. This entry is omitted for bimodal distribution cases
9	Length	Mean fan length in meters calculated from the fan length histogram for the entire HiRISE image
10	Speed	Wind speed estimate in m s^{-1} calculated from fan lengths, given the assumptions discussed in the paper

Note. If a value is missing in the file, it means that the value has not been retrieved, most probably because the fit to the P4 data was unsuccessful.

(This table is available in its entirety in machine-readable form.)

Appendix B
Additional Figures for P4 ROIs

Figures 28–32 show examples of plots and maps that were created for P4 ROIs to support the analysis presented in this paper. The plots utilize P4 data, HiRISE, CTX, and MOLA data, as well as simulated wind data from MRAMS.

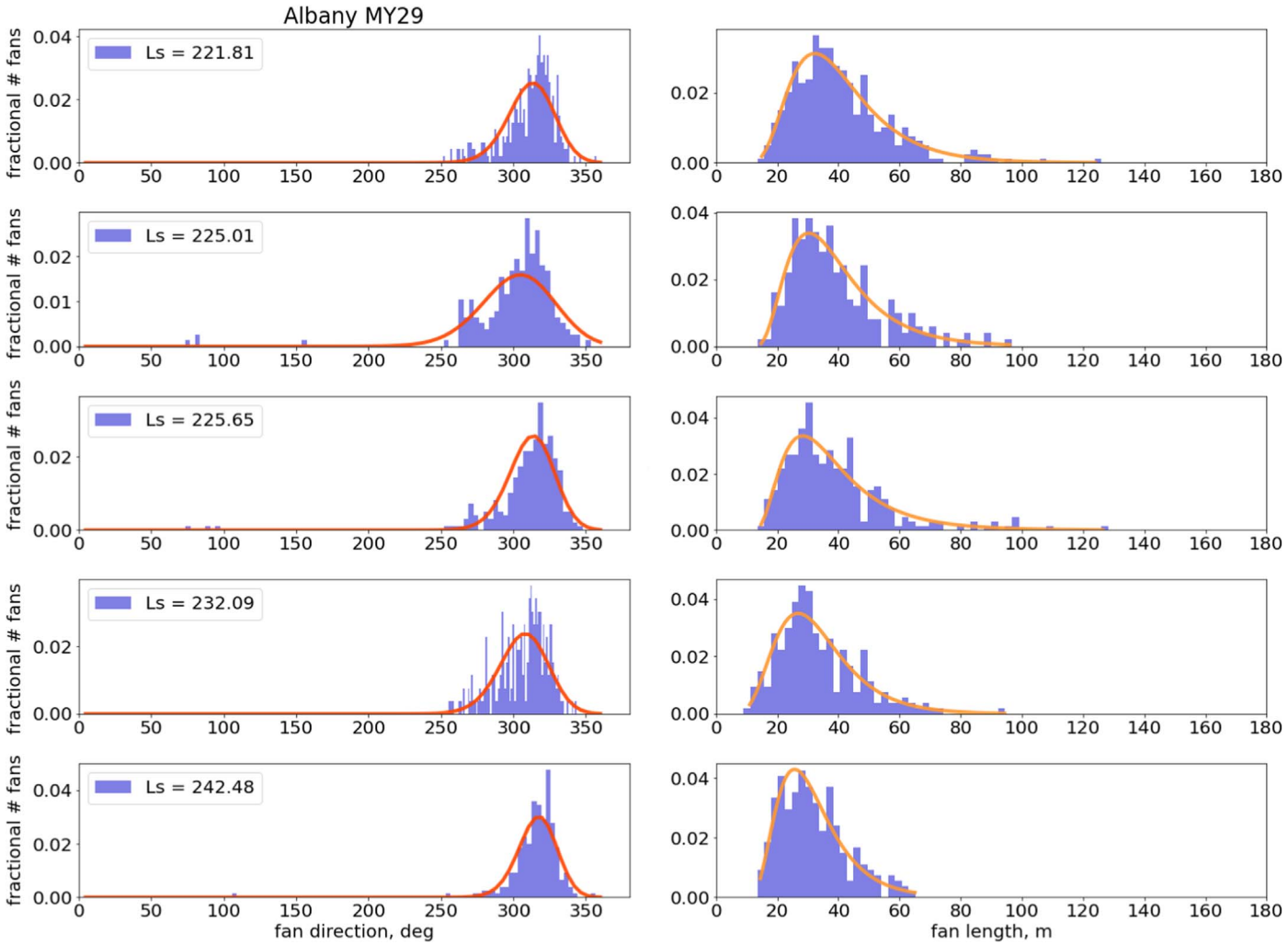

Figure 28. An example of histogram plots in ROI Albany. Blue histograms show distributions of P4-derived fan directions (left panels) and fan lengths (right panels) in each ROI for multiple HiRISE images acquired at L_s indicated on each plot frame. For histograms with single mode distributions, red or orange curves are Weibull function fits used to quantify the prevailing fan direction and length for each HiRISE image. If a histogram shows bimodal distribution, then they were fitted with a curve that combines two Gaussian curves (shown in magenta). If P4 data statistics was poor and successful fit was not possible, then no curve is present in the plot. The ROI name and Martian year (MY) for which the original HiRISE data were acquired are indicated in title on the top left. Two values for MY here represent MY of the first and last plots in the figure. A single ROI can span over multiple figures depending on the number of HiRISE images processed by P4. The complete figure set (39 images) is available in the online journal.

(The complete figure set (39 images) is available.)

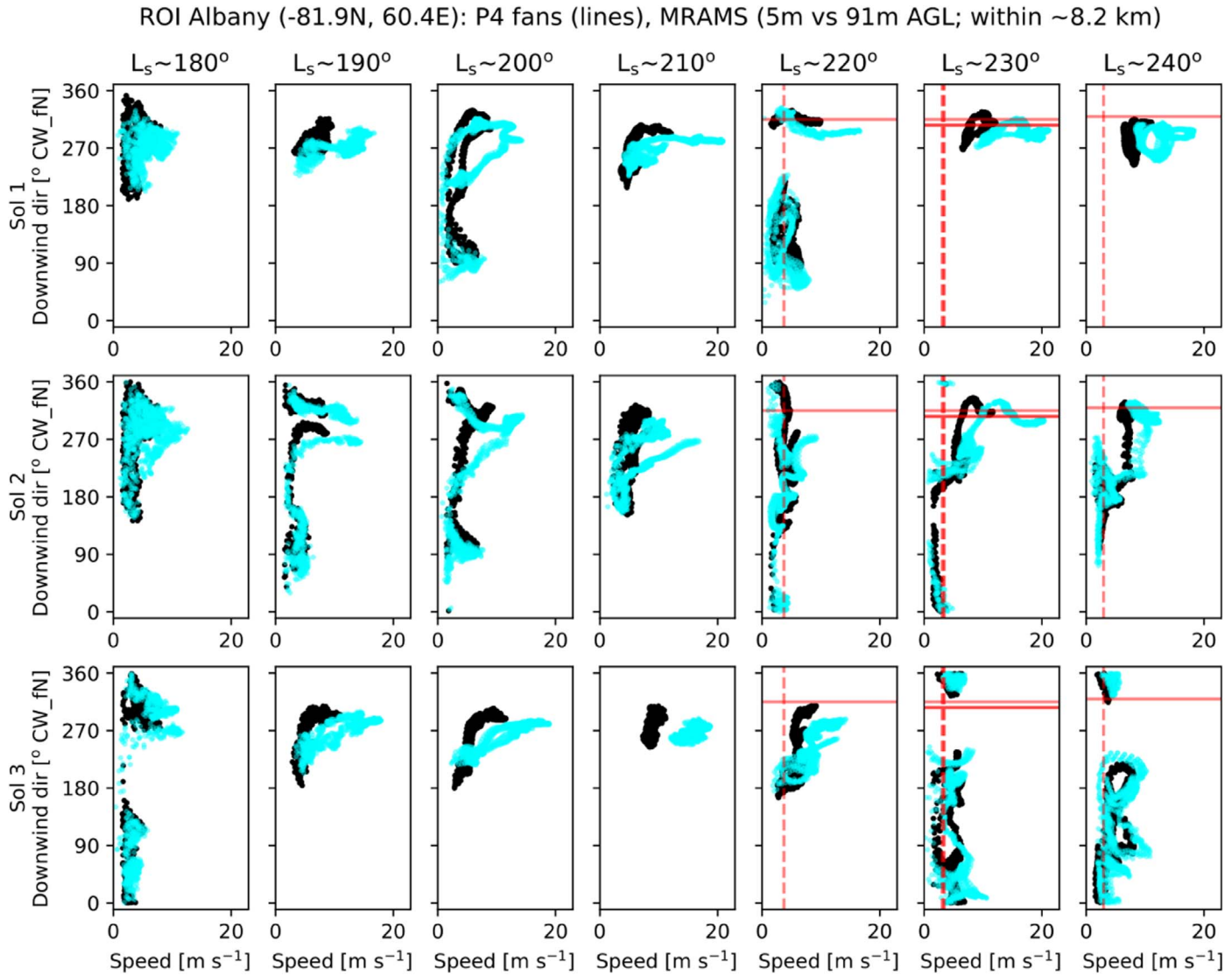

Figure 29. P4–MRAMS comparison in ROI Albany for 3 consequent sols in the MRAMS simulation run. Each column is a 10° step in L_s, and each row represents 1 sol. Panels show scatter plots of downwind directions and speeds from MRAMS, with values from ~5 m AGL shown in black and those from ~91 m shown in cyan, indicating the level of wind velocity variance within the lowest 100 m of the atmosphere. All horizontal grid points within 8.3 km of the ROI centroid are shown. Solid horizontal red lines indicate fan directions derived from P4 results, and dashed vertical red lines indicate wind speeds estimated from P4 results. Several lines in one L_s bin indicate that multiple HiRISE images acquired during this L_s period were measured by P4. The complete figure set (22 images) is available in the online journal.

(The complete figure set (22 images) is available.)

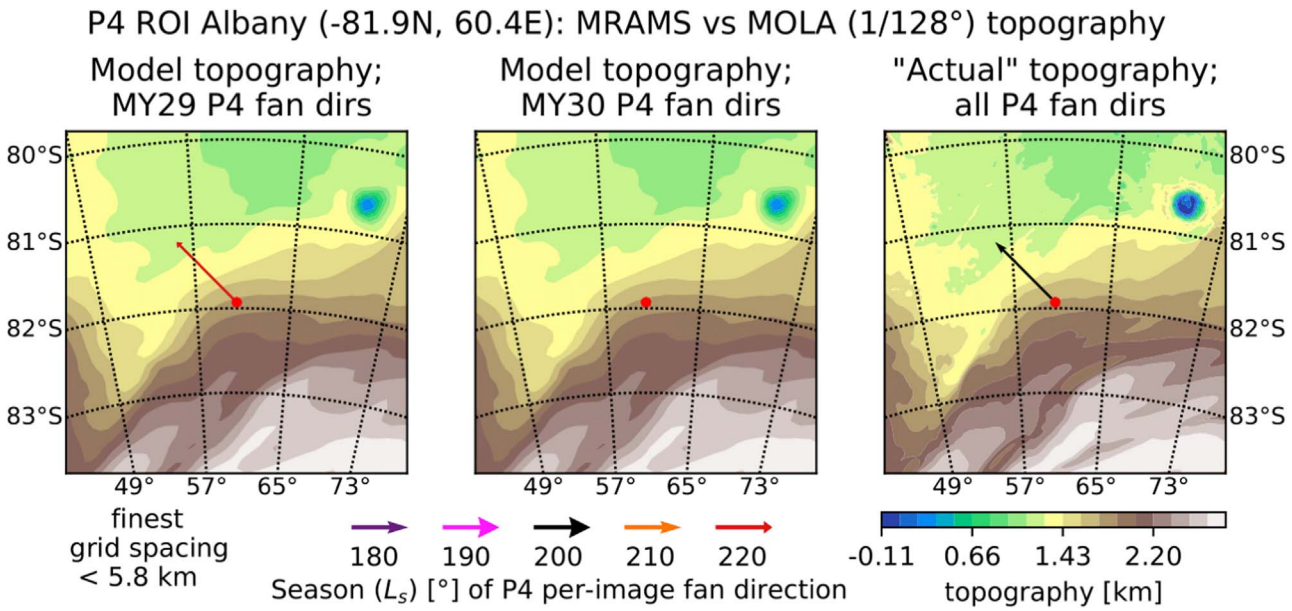

Figure 30. Topography for ROI Albany (an approximately 240 km × 240 km area). Plots of this type consist of three panels: The left panel shows the topography used by the MRAMS model overlaid with arrows that represent wind directions derived from P4 data for MY29. Arrows that show P4 data are color-coded for L_s ranges. The middle panel is the same but shows P4 data for MY30. In the right panel is the best resolution topography map available for this area. All panels cover approximately 240 km × 240 km area around the center of HiRISE images taken in this ROI. The complete figure set (21 images) is available in the online journal.

(The complete figure set (21 images) is available.)

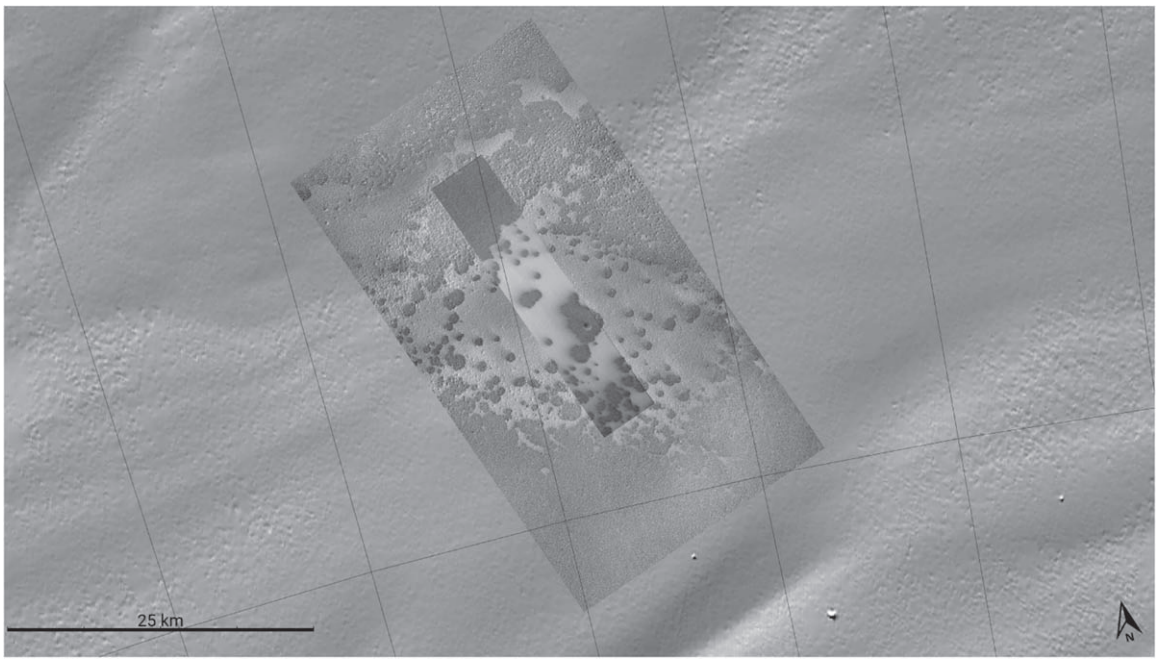

Figure 31. Context of ROI Albany. In context images the background image is MOLA shaded topography, the first insert is a CTX context image, and the narrowest highest-resolution insert is a HiRISE image taken in spring. Meridian lines are spaced 2° apart. Direction to north is noted by the arrow in the lower right corner. In this example, the first insert is CTX context image (G12_022998_0982_XN_81S293W) and the narrowest highest-resolution insert is HiRISE ESP_020374_0980_RED. The complete figure set (21 images) is available in the online journal.

(The complete figure set (21 images) is available.)

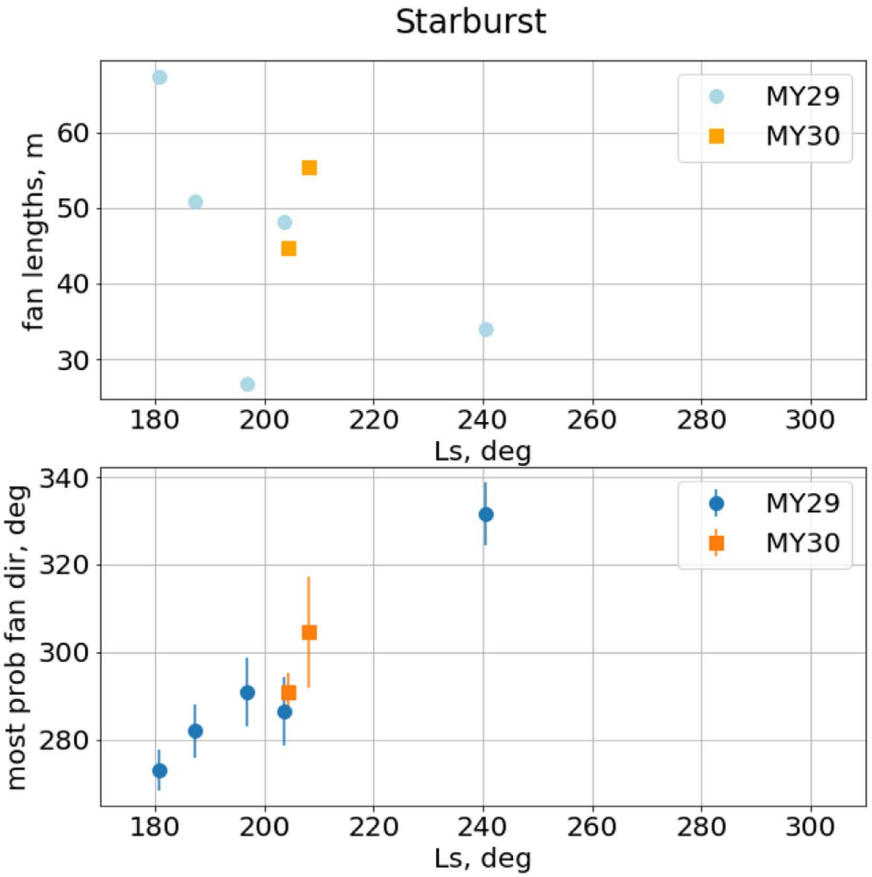

Figure 32. Prevailing P4-derived fan length (top panel) and directions (bottom panel) vs. L_s during local spring in ROI Starburst are compared for MY29 and MY30. To visualize the width of the fan direction histograms, we use error bars in the bottom panel. They should serve as a measure of the variability of P4 markings over a single HiRISE image, and they do not provide quality evaluation for the measurement made, i.e., they are not actual error bars. These types of plots are only included for selected ROIs that have good temporal coverage over L_s. The complete figure set (7 images) is available in the online journal.

(The complete figure set (7 images) is available.)

ORCID iDs

Ganna Portyankina https://orcid.org/0000-0002-1323-8195
Klaus-Michael Aye https://orcid.org/0000-0002-4088-1928
Megan E. Schwamb https://orcid.org/0000-0003-4365-1455
Candice J. Hansen https://orcid.org/0000-0001-5863-299X
Chris J. Lintott https://orcid.org/0000-0001-5578-359X

References

Aye, K. M., Schwamb, M. E., Portyankina, G., et al. 2019, Icar, 319, 558
Chojnacki, M., Burr, D. M., Moersch, J. E., & Michaels, T. I. 2011, JGRE, 116, E00F19
Christensen, P. R., Bandfield, J. L., Hamilton, V. E., et al. 2001, JGR, 106, 23823
Cunningham, E. 1910, RSPSA, 83, 357
de Villiers, S., Nermoen, A., Jamtveit, B., et al. 2012, GeoRL, 39, L13204
Georgelin, M., Richard, E., Petitdidier, M., & Druilhet, A. 1994, MWRv, 122, 1509
Haberle, R. M., Houben, H. C., Hertenstein, R., & Herdtle, T. 1993, JAtS, 50, 1544
Haberle, R. M., Kahre, M. A., Hollingsworth, J. L., et al. 2019, Icar, 333, 130
Hansen, C. J., Aye, K.-M., Portyankina, G., & Schwamb, M. E. 2019, LPSC, 50, 3110
Hansen, C. J., Thomas, N., Portyankina, G., et al. 2010, Icar, 205, 283
Hayne, P. O., Paige, D. A., & Heavens, N. G. 2014, Icar, 231, 122
Hébrard, E., Listowski, C., Coll, P., et al. 2012, JGRE, 117, E04008
Kieffer, H. H. 2007, JGR, 112, E08005
Kieffer, H. H., Christensen, P. R., & Titus, T. 2006, Natur, 442, 793
Leighton, R. B., & Murray, B. C. 1966, Sci, 153, 136
Malin, M. C., Danielson, G. E., Ingersoll, A. P., et al. 1992, JGRE, 97, 7699
Malin, M. C., & Edgett, K. S. 2007, JGR, 106, 23429
Mason, P. J. 1991, in Workshop Proc. on Fine Scale Modelling and the Development of Parameterization Schemes (ECMWF), 275
Matsuo, K., & Heki, K. 2009, Icar, 202, 90
McEwen, A. S., Eliason, E. M., Bergstrom, J. W., et al. 2007, JGRE, 112, E05S02
Michaels, T. I., Colaprete, A., & Rafkin, S. C. R. 2006, GeoRL, 33, L16201
Michaels, T. I., & Rafkin, S. C. R. 2008, JGRE, 113, E00A03
Pike, W. T., Staufer, U., Hecht, M. H., et al. 2011, GeoRL, 38, L24201
Piqueux, S., Byrne, S., & Richardson, M. I. 2003, JGRE, 108, 5084
Piqueux, S., & Christensen, P. R. 2008, JGR, 113, E06005
Portyankina, G., Markiewicz, W. J., Thomas, N., Hansen, C. J., & Milazzo, M. 2010, Icar, 205, 311
Putzig, N. E., & Mellon, M. T. 2007, Icar, 191, 68
Rafkin, S. C. R., Haberle, R. M., & Michaels, T. I. 2001, Icar, 151, 228
Rafkin, S. C. R., & Michaels, T. I. 2003, JGRE, 108, 8091
Rafkin, S. C. R., & Michaels, T. I. 2019, Atmos, 10, 747
Rafkin, S. C. R., Sta Maria, M. R., & Michaels, T. I. 2002, Natur, 419, 697
Schmid, O., Trueblood, M. B., Gregg, N., Hagen, D. E., & Whitefield, P. D. 2002, AerST, 36, 351
Smith, D. E., Zuber, M. T., Frey, H. V., et al. 2001, JGR, 106, 23689
Smith, M. D. 2004, Icar, 167, 148
Thomas, N., Hansen, C. J., Portyankina, G., & Russell, P. S. 2010, Icar, 205, 296
Thomas, N., Portyankina, G., Hansen, C., & Pommerol, A. 2011, Icar, 212, 66